Hexagonal Majorana fermion lattice constructed from topological insulator Josephson junctions

master's thesis

Submitted to the Faculty of Mathematics, Computer Science and Natural Sciences at RWTH Aachen University

presented by

Anton Montag

under the supervision of

Prof. Dr. Fabian Hassler

and

Prof. Dr. Markus Müller

Institute for Quantum Information

07/2023

Abstract

In this thesis, we discuss the realization of a hexagonal Majorana fermion lattice and its thermal transport properties. We analyze the two-dimensional Josephson junctions on the surface of topological insulators to obtain topological Majorana wires in the low-energy regime. Using this description of the wires, we construct trijunctions and derive three distinct topological phases of them, two of which host Majorana bound states. We connect multiple Majorana bound states with topological insulator Josephson junctions to a hexagonal lattice of Majorana fermions. The spectrum of this lattice is calculated, the appearance of edge states is shown, and the scaling behavior of the thermal conductance of the hexagonal Majorana lattice is analyzed.

Contents

List of Figures

Chapter 1

Introduction

Majorana fermions were first conceived in 1937 [1] in the context of particle physics, as a particle, which is its own anti-particle and otherwise is closely related to fermions. Later, it was discovered, that Majorana fermions could appear as emergent excitations in solid-state systems. These quasiparticle excitations are especially interesting, because they do not obey fermionic exchange statistics, but behave like 'non-Abelian anyons' [2]. The exchange of two Majorana fermions is called braiding, since the order of exchanging particles matters for non-Abelian anyons. Quantum algorithms can be realized by braiding Majorana fermions, and therefore the observation of Majorana modes in solid state systems is of great interest, but until this day there is no experimental verification of the existence of Majorana zero modes.

There are many theoretical proposals, which should host localized Majorana zero modes, and they share two properties. First, the system needs to be superconducting, in order to be able to host excitations with the properties of Majorana fermions [3]. Since the Majorana mode cannot carry charge, it has to be a coherent superposition of particle and hole state, which occurs naturally in the theory of superconductivity. The second condition is, that the system exhibits topological phase transitions, where a band-gap closes and reopens again. There are many proposed systems with these properties [4, 5], but we focus on topological insulators.

Starting from the discovery of the quantum hall effect in 1980 [6], new states of matter were discovered, which are topologically distinct from states of matter known before. These types of materials have a gapped spectrum and exhibit properties, which stay invariant unless the band gap closes. Each of these invariant quantities defines a topological phase, and only band closings give rise to topological phase transitions. The most important property for this thesis is the appearance of boundary states between different topological domains. These boundary states are also appearing at the edges of systems in the topological phase, and have a spectrum, which is not part of the bulk spectrum, but lies in the band gap of the bulk. We use these special edge states of three dimensional topological insulators to realize Majorana fermions of the two-dimensional surface.

By proximitizing the topological insulator surface with superconducting materials we obtain a two-dimensional system with the special properties of the topological edge states and tunable superconductivity. It is known, that in this system Majorana bound states can appear in magnetic vortices, but we follow a different approach, where we consider narrow two-dimensional Josephson junctions on the surface [7]. In such a Josephson junction, two superconducting regions are separated by a narrow strip of bare topological insulator surface. We will show, that these junctions act like a wire for propagating Majorana modes and that we can obtain Majorana bound states at trijunctions of these wires. Finally, we will consider a network of such trijunctions connected by Josephson junctions and show, that we can realize a hexagonal lattice of Majorana fermions with such a network. We will analyze the spectrum and transport properties of this lattice and investigate the scaling behavior of thermal conductance in the presence of fluctuations in the lattice.

This thesis is organized as follows. In Ch. 2 we will introduce Majorana fermions and show their properties. Further we will give a brief introduction into the field of topology in condensed matter physics and introduce important concepts for this thesis. We will show the emergence of edge states in a simplified one-dimensional system and use this, to obtain the surface description of a simplified three-dimensional Bernevig-Hughes-Zhang model [8]. Afterwards, we will explain important results of the Bardeen-Cooper-Schrieffer theory of superconductivity. We will show the appearance of the pairing gap and explain the proximity effect for superconductor interfaces. For the description of the proximitized topological insulator surface, we will introduce the Bogoliubov-de Gennes formalism. Finally, we will motivate Andreev bound states in Josephson junctions and show, how gauge fields affect superconducting systems. Building on the description of a proximitized topological insulator surface, we will follow the idea of a topological insulator Josephson junction [7] in Ch. 3. We will derive the emergence of propagating Majorana modes and calculate their effective one-dimensional wire Hamiltonian. Further we will investigate, how disorder in the systems affects the Majorana wire and prove, that the Majorana wire has two distinct topological phases.

Using the previous results, we will construct trijunctions of three Majorana wires in Ch. 4. For these trijunctions, we will derive three different topological phases, out of which two host a Majorana bound state localized at the trijunction. We will derive a complete phase diagram for the trijunction and introduce a topological invariant for this system. In Ch. 5 we will construct a hexagonal lattice of Majorana fermions, where we will connect different trijunctions by Majorana wires leading to a nearest-neighbor interaction in the lattice. We will calculate the spectrum of the lattice analytically for a clean lattice, and show, how fluctuations of the superconducting pairing gaps effect the Majorana lattice Hamiltonian. For numerical simulations we will introduce a transformation of the Majorana lattice into a superconducting fermionic lattice. One-dimensional transport spectra will be calculated, and there we will show the appearance of edge states. Finally, we will analyze the thermal conductance through the lattice and how it scales for disordered systems. We will end with a conclusion and an outlook on possible research directions following up on the presented work.

Chapter 2

Theoretical background

This chapter introduces the basic physical concepts used in this thesis. We start by defining Majorana fermions and show their main properties. We are not only interested in the properties of a Majorana lattice, but also want to show, how a lattice like this can be realized theoretically. Hence, we will not start with a Hamiltonian for the hexagonal Majorana lattice right away, but derive the the emergence of Majorana bound states instead. We will focus on topological superconducting systems as a platform for Majorana bound states. To describe these platforms, we give a brief introduction into topology in condensed matter physics. There we will focus on the most basic concepts of topological invariants and bulk-edge correspondence needed for the derivation of the Majorana lattice later in the thesis. In the derivation of the Majorana bound states, the topological material is needed for its special surface properties. We will show how the low-energy regime of the surface of a topological insulators shows similarities to a massless Dirac fermion with a dispersion relation that is linear in momentum. Since the special surface properties are tied to the bulk properties of the topological insulator, we have to start from a simple model of a three-dimensional topological insulator and obtain the surface states using the Jackiw-Rebbi model, which will also be introduced in this chapter. Further, we need the topological surface to be superconducting to generate Majorana bound states later, thus we will introduce superconductivity. After a brief review of the main results of the Bardeen-Cooper-Schrieffer theory of superconductivity we will explain the proximity effect, that can introduce superconductivity in the topological surface derived before. For the description of the superconducting surface we will use the Bogoliubov-de Gennes formalism. From this Hamiltonian we will be able to calculate Majorana bound states in special arrangements of superconductors. However, to describe the properties of a lattice we need to describe the behavior of propagating Majorana modes in junctions between superconductors. For this propagation we will need gauge theory for superconducting systems and we need to know how the low-energy propagating modes couple to higher bound states in such a junction. In the last two sections of this chapter we will describe these topics briefly.

2.1 Majorana fermions

The lattice, which we are considering in this thesis, is a tight-binding model of Majorana fermions. While the first part of the thesis is focused on the realization of such a lattice and most of the background provided in this chapter is relevant for that, we want to start by giving an overview of the properties of Majorana fermions.

Majorana fermions were first proposed in high energy physics [1] as solutions of the Dirac equation. The main idea was a particle, which resembles many properties of a fermion, but is its own anti-particle. If the annihilation operator for one Majorana fermion is denoted by γ_i, this property yields

$$\gamma_i = \gamma_i^\dagger \quad \text{and} \quad \gamma_i^2 = 1\,. \tag{2.1}$$

Different Majorana fermions anti-commute, and with the condition in Eq. (2.1) the anti-commutation relations are given by

$$\{\gamma_i, \gamma_j\} = 2\delta_{i,j}\,. \tag{2.2}$$

In condensed matter physics, particles with these properties can appear as quasiparticle excitations in superconducting systems [3]. We will show this for a topological insulator Josephson junction in Ch. 3.

To get a first insight, how Majorana particle emerge in condensed matter systems, we show that truly fermionic operators c_i and $c_i^\dagger$ can be transformed into a Majorana basis. The fermionic operators obey

$$\left\{c_i, c_j^\dagger\right\} = \delta_{i,j} \quad \text{and} \quad \{c_i, c_j\} = 0 \tag{2.3}$$

and can be decomposed into Majorana operators. We need two Majorana operators $\gamma_{i\alpha}$ with $\alpha = 1, 2$ to decompose a pair of adjoint pair of fermionic operators The creation and annihilation operators are then given by

$$c_i^\dagger = \tfrac{1}{2}\left(\gamma_{i1} + i\gamma_{i2}\right) \quad \text{and} \quad c_i = \tfrac{1}{2}\left(\gamma_{i1} - i\gamma_{i2}\right)\,. \tag{2.4}$$

If $\gamma_{i\alpha}$ obeys the Majorana relations, then the commutation relations for the fermionic operators are fulfilled. The inverse transformation is given by

$$\gamma_{i1} = c_i + c_i^\dagger \quad \text{and} \quad \gamma_{i2} = i\left(c_i - c_i^\dagger\right) . \tag{2.5}$$

This coherent superposition of electron and hole degrees of freedom shows why Majorana fermions emerge in superconducting systems. There, this coherent superposition occurs naturally, which will be shown in the chapter on Bardeen-Cooper-Schrieffer theory. Localized Majorana states appear for example at the domain walls between different phases of topological superconductors [9] or in magnetic vortices in topological insulator-superconductor heterostructures [4]. In both cases, the topology of the system is important for the emergence of Majorana fermions. In the next section, we will introduce topology in the context of condensed matter physics and discuss two important models for our work.

2.2 Introduction into topology

In this section we want to give a brief introduction into topology. The research field of topology in condensed matter physics is vast and there are many important results. A formal and much more complete introduction of topology is given by Qi and Zhang [10]. We will only motivate topological effects and introduce the concept of a topological invariant that classifies different topological phases. Further, we will explain the principle of bulk-edge correspondence and show a method of deriving boundary states between different topological phases. Afterwards, we will describe a model for a three-dimensional topological insulator and derive the surface states. We will use this model to construct the topological insulator Josephson junction, from which we will construct the Majorana lattice.

The first time a topological effect was measured, was the discovery of the quantum Hall effect by von Klitzing *et al.* [6], later explained by Laughlin [11] and Thouless *et al.* [12]. The edge of a two-dimensional bulk insulating material carries a Hall current, whose conductance is quantized to integer values of e^2/h. This does not depend on microscopic details of the material, but can be viewed as a topological charge pump. Later many more systems with much more complicated or subtle topological properties were discovered and topology in condensed matter had to be formalized.

Topological equivalence classes are defined for gapped systems, where the ground state is separated from the excited states by an energy gap. If the spectra for such systems can be continuously deformed into each other without closing the energy gap, they belong to the same equivalence class. If there is no deformation that achieves this, the systems must belong to different equivalence classes, which are also called topological phases.[1] For a phase transition a closing of the energy gap is necessary. How the classes can be distinguished by topological invariants and what happens on the interface between different topological phases, will be discussed in the next section.

2.2.1 Topological invariants and bulk-edge correspondence

Topological invariants are a method to characterize different topological phases by a measurable quantity. The invariant has to be different for all possible phases. It is only allowed to change, if a band gap closes in the system, and it cannot depend on microscopic details of the Hamiltonian. Such quantities can be expressed as invariant integrals over momentum space. Sometimes this property is called bulk-topological invariant, since one can calculate it from the bulk spectrum of the topological system alone. For the models we use, this invariant is always a so-called $\mathbb{Z}_2$, which can only take the values ± 1. The models only show two different phases, from which one is denoted as topological and one trivial.

Another property of topological matter is the bulk-edge correspondence. If matter in two different topological phases is brought into contact, the interface between the two domains can host special states. In one dimension, these states are localized at the domain wall and in higher dimensions these boundary states are gapless states. This property of topological matter is called bulk-edge correspondence, because it also occurs on the boundary between a topological material and the vacuum. The vacuum is always thought of as a trivial insulator. If there is a material in a topological phase, the edge of the material becomes a domain wall between different topological phases. This domain wall will host states that are called edge or surface states of the system. Any material where the edge of a system supports boundary states is topological and any material without boundary states is trivial. The appearance of edge states is an example of bulk-edge correspondence. The topological invariant, which is a bulk property has to change, if there is a phase transition where the boundary

[1]This continuous deformation is the reason why the phases are called 'topological'. The term is taken from mathematics, where topology is concerned with the continuous deformation of geometric objects.

behavior changes.

For the systems we consider, the boundary states are always described by a Dirac Hamiltonian.[2] If we have a one-dimensional or two-dimensional system where $\boldsymbol{\sigma}$ act on a two-level degree of freedom, the Dirac Hamiltonian is given by

$$H_{\text{Dirac}} = v\,\boldsymbol{p}\cdot\boldsymbol{\sigma} + m\,\sigma_z \tag{2.6}$$

with $\boldsymbol{p} = p_x\hat{e}_x$ in the one-dimensional and $\boldsymbol{p} = (p_x, p_y)^T$ in the two dimensional case. The term $m\,\sigma_z$ is called mass term[3] and v is usually called Dirac velocity. The spectrum of such a Dirac Hamiltonian is always given by

$$E_k = \pm\sqrt{v^2\boldsymbol{p}^2 + m^2}\,. \tag{2.7}$$

Without a mass term the spectrum is gapless, and therefore we expect the surface Hamiltonian to have a vanishing mass $m = 0$. To calculate such a surface Hamiltonian, we will use the Jackiw-Rebbi model, which solves a one-dimensional topological model. We will show, how we can use this to obtain a surface Hamiltonian for a three-dimensional topological insulator, described by the Bernevig-Hughes-Zhang model.

2.2.2 Jackiw-Rebbi model

Here we introduce a simple model describing the appearance of zero energy states at the boundary between different topological domains. This model was first introduced by Jackiw and Rebbi for studying solutions in quantum field theory [13]. The simple one-dimensional model can also be used to derive the surface spectrum of higher dimensional topological insulators.

We use a toy model h, that is a simplified version of the original model. We consider a one dimensional Dirac Hamiltonian

$$h = v\,p_x\cdot\sigma_x + m(x)\,\sigma_z \tag{2.8}$$

with real parameters v and m. The Pauli operators $\boldsymbol{\sigma}$ act on some degree of freedom that can be a physical spin, a two-level orbital structure or particle-hole space. To include all possibilities, we use $\boldsymbol{\Psi} = (\Psi_1, \Psi_2)$ as general basis.

[2]The Dirac Hamiltonian usually describes the behavior of fermions in high energy physics. We use the term here, since the structure of the Dirac Hamiltonian is the same as for the surface states.

[3]In the one-dimensional case, the mass term can also enter proportional to σ_y instead of σ_z. The only condition is, that it anti-commutes with all momentum dependent terms in k-space.

Eq. (2.8) is a one-dimensional topological model, and the topological invariant is the sign of the mass term m. The spectrum is given by

$$E_k = \pm\sqrt{(vk)^2 + m^2} \tag{2.9}$$

with k as momentum quantum number. The two bands are separated by a band gap $2m$, and this gap closes at $m = 0$. The topological phase transition from the topological phase $m < 0$ to the trivial phase $m > 0$ can be found at the band closing.

Now we consider a position-dependent mass $m(x)$, that has to be a real integrable function of x. We choose the mass, such that we model a domain wall between different topological domains. The constraints, that need to be fulfilled, are $\lim_{x\to\pm\infty} m(x) = m_\pm \neq 0$ and that there is only one point x_0 where $m(x)$ changes sign. The claim is, that there is always a zero-energy solution localized at the domain wall x_0. To prove this, we rearrange the Schrödinger equation for h with $m = m(x)$, such that the derivative is isolated. Use $\sigma_i^2 = \sigma_0 = \mathcal{I}_2$ [4] to isolate the partial derivative appearing in the momentum p_x. The Schrödinger equation can now be rearranged to

$$h\,\mathbf{\Psi} = 0 \implies \partial_x\,\mathbf{\Psi} = -\frac{m(x)}{v}\sigma_y\,\mathbf{\Psi}\,. \tag{2.10}$$

Now we assume the wave function is an eigenstate $\boldsymbol{\chi}_y = 1/\sqrt{2}\,(1, \pm i)^T$ of σ_y with the eigenvalue $\lambda_y = \pm 1$. Then the full wave function is $\mathbf{\Psi} = \boldsymbol{\chi}_y \cdot f(x)$, where $f(x)$ is a scalar function. Inserting this in Eq. (2.10) yields a differential equation for $f(x)$, which is solved by

$$\partial_x f(x) = -\lambda_y\,\frac{m(x)}{v}\,f(x) \implies f(x) = \frac{1}{\sqrt{N}}\cdot e^{-\lambda_y/v\int_{x_0}^{x} m(\tilde{x})d\tilde{x}}\,. \tag{2.11}$$

The solution $f(x)$ has to be normalizable to yield a zero energy solution of the Schrödinger equation in Eq. (2.10). This is the case for $\lambda_y = \mathrm{sgn}(m_\infty)$, where $N = \int |f(x)|^2 dx$ is finite due to the exponential suppression at both ∞ and $-\infty$. The zero energy solution is given by

$$\mathbf{\Psi} = \frac{1}{\sqrt{2N}}\,(1, \mathrm{sgn}(m_\infty)\cdot i)^T \cdot e^{-\mathrm{sgn}(m_\infty)/v\int_{x_0}^{x} m(\tilde{x})d\tilde{x}}\,. \tag{2.12}$$

[4] In this thesis all identity matrices $\mathcal{I}_2$ are dropped in the notation of any Hamiltonian and any tensor product.

The zero-energy state is localized at x_0 in the sense, that the probability density $|\boldsymbol{\Psi(x)}|^2$ is maximal at x_0 and decays for increasing $|x - x_0|$. The shape of the probability density depends on $m(x)$, but under the conditions stated above, there always exists a zero energy solution. This approach of solving for zero energy solutions of a Hamiltonian is referred to as Jackiw-Rebbi approach, and it will be used to derive the surface Hamiltonian of a three dimensional topological insulator in the next section.

2.2.3 BHZ-model for a three-dimensional topological insulator

We need a two dimensional topological insulator surface to construct the Josephson junction and the Majorana lattices. For this surface a three dimensional bulk topological insulator is needed. We use the three dimensional Bernevig-Hughes-Zhang model introduced by Zhang *et al.* [8], building on earlier work by Bernevig, Hughes and Zhang [14]. In the basis $\boldsymbol{\Psi} = ((\Psi^1_\uparrow, \Psi^1_\downarrow), (\Psi^2_\uparrow, \Psi^2_\downarrow))^T$, where $i = 1, 2$ is denoting the orbital and $\updownarrow$ the spin, the Hamiltonian is given by

$$H_{\mathrm{BHZ}} = (\varepsilon_0(\boldsymbol{k}) - \mu) + M(\boldsymbol{k})\,\hat{\pi}_z + A_1\,k_z\,\hat{\pi}_x\hat{\sigma}_z + A_2(k_x\hat{\pi}_x\hat{\sigma}_x + k_y\,\hat{\pi}_x\hat{\sigma}_y) \quad (2.13)$$

with

$$\varepsilon_0(\boldsymbol{k}) = C + D_1 k_z^2 + D_2(k_x^2 + k_y^2) \quad \text{and} \quad (2.14)$$

$$M(\boldsymbol{k}) = M - B_1 k_z^2 - B_2(k_x^2 + k_y^2)\,. \quad (2.15)$$

The Pauli operators $\hat{\boldsymbol{\pi}}$ act on the orbital degree of freedom and $\hat{\boldsymbol{\sigma}}$ on the spin degree of freedom. In our notation tensor products of different Pauli operators are always implied, and identity operators acting are not written explicitly, but are implied, if a degree of freedom is missing from a term. The parameters M, A_j, B_j, C and D_j are real and can be used to fit H_{BHZ} to a real material.

For our purposes we use the simplest version of the model in Eq. (2.13) that exhibits a topological phase transition. We neglect the spin and orbital independent part of the spectrum $\varepsilon_0(\boldsymbol{k})$ by setting $C = D_j = 0$ and choose

$$A_1 = A_2 = v \quad \text{and} \quad B_1 = B_2 = \frac{v}{2|M|}\,. \quad (2.16)$$

With this choice of parameters, the Hamiltonian simplifies to

$$H_{\mathrm{BHZ}} = -\mu + (M - \frac{v}{2|M|}\,\boldsymbol{k}^2)\hat{\pi}_z + v\hat{\pi}_x\,\boldsymbol{k}\cdot\hat{\boldsymbol{\sigma}}\,. \quad (2.17)$$

It can be shown that for this choice of parameters, the trivial phase is given by $M < 0$ and the topological phase by $M > 0$.[5]

The bulk spectrum can be easily calculated using the fact, that for any Pauli degree of freedom $\boldsymbol{\alpha}$, the relation $(\boldsymbol{d} \cdot \boldsymbol{\alpha})^2 = \boldsymbol{d}^2\, \alpha_0$ is valid. We square $H_{\mathrm{TI}} + \mu$ and obtain

$$(H_{\mathrm{TI}}+\mu)^2 = \left(M - \frac{v^2}{2|M|}\,\boldsymbol{k}^2\right)^2 + (v\boldsymbol{k})^2 = \left(M^2 + \frac{(v\boldsymbol{k})^2}{4M^2}\right) = \left(E_\pm(\boldsymbol{k})\right)^2 . \quad (2.18)$$

From this, we know the bulk spectrum of the simplified topological insulator model

$$E_\pm(\boldsymbol{k}) = \pm\sqrt{M^2 + \frac{(v\boldsymbol{k})^2}{4M^2}}\,. \quad (2.19)$$

The resulting bulk gap is $2|M|$, independent of the sign of M. The topological insulator is therefore always gapped in both phases, and only at the phase transition $M = 0$ the bulk gap closes. The magnitude of the bulk gap of the topological insulator is used as a reference energy to compare energy scales later.

To obtain the surface spectrum in the topological phase, we model a topological insulator-vacuum interface by varying the mass term. To model a boundary between the two regions in different topological phases, the sign of $M(z)$ has to change at the domain wall. For a surface in x-y-plane we use the function

$$M(z) = \begin{cases} M_{\mathrm{TI}} > 0 & z \leq 0 \\ M_{\mathrm{vac}} = -\infty & z > 0 \end{cases}, \quad (2.20)$$

which simplifies calculations. The Hamiltonian given by Eq. (2.17) is expanded up to first order in all k_i. The reasoning behind this is, that we expect low energy bound states located at the domain wall. Therefore higher order momentum terms can be neglected and H_{TI} can now be separated to isolate the terms containing z or p_z. Since the translational invariance in z-direction is broken, k_z is not a good quantum number anymore. This is not the case for k_x and k_y, and we obtain

$$H_{\mathrm{TI}} = \underbrace{\left(M(z)\hat{\pi}_z + v p_z\, \hat{\pi}_x \hat{\sigma}_z\right)}_{H_\perp} + \underbrace{v\, \hat{\pi}_x \left(k_x \hat{\sigma}_x + k_y \hat{\sigma}_y\right) - \mu}_{H_\parallel} . \quad (2.21)$$

[5] In this simplified model, the sign in front of the quadratic momentum term $\boldsymbol{k}^2$ is defining the sign of the M for the vacuum, which is always defined to be a trivial insulator. We do not prove this here.

The first term $H_\perp$ is a Jackiw-Rebbi model perpendicular to the surface. It can be solved exactly for zero-energy states, and since two Pauli matrices appear in a tensor product, there must be two zero-energy surface states. This is due to the fact that both eigenvalues ± 1 of a tensor product of n Pauli matrices are n-fold degenerate. Here the Jackiw-Rebbi model reduces to the eigenvalue problem

$$\hat{\pi}_y \hat{\sigma}_z \, \boldsymbol{\chi}_i = -1 \boldsymbol{\chi}_i \tag{2.22}$$

for the two eigenvectors $\boldsymbol{\chi}_i$ with $i = 1, 2$ and the partial differential equation

$$\partial_z f(z) = -\frac{M(z)}{v} f(z) \,. \tag{2.23}$$

Then the zero-energy solutions of $H_\perp$ are given by

$$\boldsymbol{\Psi}_i^\perp = \frac{1}{\sqrt{N}} \boldsymbol{\chi}_i \cdot f(z) = \sqrt{\frac{M_{\mathrm{TI}}}{v}} \, \Theta(-z) \, e^{\frac{M_{\mathrm{TI}}}{v} z} \cdot \begin{cases} (1, 0, -i, 0)^T & i = 1 \\ (0, -i, 0, 1)^T & i = 2 \end{cases} . \tag{2.24}$$

The choice of $M_{\mathrm{vac}} = -\infty$ restricts the wave function to live only in the topological insulator. The surface states decay exponentially into the bulk of the topological insulator.

With the two degenerate surface states, we derive the low energy surface Hamiltonian of the simplified Bernevig-Hughes-Zhang model. The zero energy surface states are the ground states of the surface and $H_\|$ from Eq. (2.21) is included as a perturbation to the degenerate ground state. Using degenerate perturbation theory, this yields an effective Hamiltonian H_{surface} acting on the Hilbert space spanned by $\boldsymbol{\Psi}_\mathbf{1}^\perp$ and $\boldsymbol{\Psi}_\mathbf{2}^\perp$. For the calculation three expectation values are evaluated and the surface Hamiltonian is given by

$$H_{\mathrm{surface}} = \begin{pmatrix} \langle \boldsymbol{\Psi}_1^\perp | H_\| | \boldsymbol{\Psi}_1^\perp \rangle & \langle \boldsymbol{\Psi}_1^\perp | H_\| | \boldsymbol{\Psi}_2^\perp \rangle \\ \langle \boldsymbol{\Psi}_2^\perp | H_\| | \boldsymbol{\Psi}_1^\perp \rangle & \langle \boldsymbol{\Psi}_2^\perp | H_\| | \boldsymbol{\Psi}_2^\perp \rangle \end{pmatrix} . \tag{2.25}$$

The expectation values are given by

$$\left\langle \boldsymbol{\Psi}_1^\perp \middle| H_\| \middle| \boldsymbol{\Psi}_1^\perp \right\rangle = -\mu = \left\langle \boldsymbol{\Psi}_2^\perp \middle| H_\| \middle| \boldsymbol{\Psi}_2^\perp \right\rangle \quad \text{and} \tag{2.26}$$

$$\left\langle \boldsymbol{\Psi}_2^\perp \middle| H_\| \middle| \boldsymbol{\Psi}_2^\perp \right\rangle = vk_x - ivk_y \,. \tag{2.27}$$

We introduce now the Pauli matrices $\boldsymbol{\sigma} = (\sigma_x, \sigma_y)^T$ that act on the two surface states $\boldsymbol{\Psi}_i^{\perp}$ and write the surface Hamiltonian in this basis as

$$H_{\text{surface}} = vk_x\sigma_x + vk_y\sigma_y - \mu = v\,\boldsymbol{p}\cdot\boldsymbol{\sigma} - \mu\,. \tag{2.28}$$

The operator $\boldsymbol{p} = (p_x, p_y)^T$ is in this case the momentum on the surface of the topological insulator. The Hamiltonian in Eq. (2.28) is a Dirac Hamiltonian without a mass, which would enter with σ_z. Accordingly there is a single Dirac cone on the surface of the topological insulator. The Pauli degree of freedom corresponds still to the spin, but here the orbital and spin degree of freedom are coupled.

Only the surface of a three-dimensional system can have a single Dirac cone, in contrast to a truly two dimensional system, where the Dirac cones appear in pairs. If one wants to simulate a system with only one Dirac cone, one can either gap out the second cone of a two dimensional Hamiltonian to avoid fermion doubling for low energies, or simulate a three dimensional topological insulator. Due to the bulk boundary correspondence, this can lift the fermion doubling problem as shown in [15], but at cost of higher computation time, since the bulk has to be simulated as well.

This method of calculating zero energy states localized in one direction and considering other terms from the full Hamiltonian will be used again later. The effective Hamiltonian is only valid for energies below the bulk gap of the system. The surface Hamiltonian is the starting point for further calculations in Ch. 3, where a two-dimensional Josephson junction is considered.

2.3 BCS theory of superconductivity

Superconductivity was first discovered by Onnes [16], when he measured the vanishing of resistance below a critical temperature. Later, the discovery of the Meissner-Ochsenfeld effect [17] led to a phenomenological description of superconductivity by F. and H. London [18]. On a microscopic level, the problem of an attractive electron-electron interaction, mediated by electron-phonon coupling, was solved by Cooper [19]. A many-body version of the Cooper-problem was solved by Bardeen, Cooper and Schrieffer [20] in a mean-field theoretical approach, which is referred to as BCS-theory. In this section, we derive the superconducting gap function and how it is effected by the gauge of the electromagnetic field. Furthermore, we show how one can describe superconductivity in the Bogoliubov-de Gennes formalism. Lastly, we briefly discuss the proximity effect.

2.3.1 Derivation of superconducting gap function

The appearance of a superconducting gap function arises from the interaction of electrons and phonons in the system. In the Hamiltonian for the electrons this results in an attractive interaction between the electrons. The criterion for superconductivity is that this attractive interaction dominates the Coulomb repulsion between electrons. The details of the electron-phonon interaction are given by Bardeen and Pines [21], and a discussion of the criterion for superconductivity in the context of BCS theory is given by Pines [22]. We are not concerned with the details of their work, instead we assume that we have a momentum-dependent attractive interaction between electrons. Furthermore, we will only consider the terms of the coupling with zero-momentum transfer. As stated in [20], other terms have only little effect on the free energy and may be treated as a perturbation.

We consider the Hamiltonian in terms of creation and annihilation operators of the electrons, that fulfill the commutation relations

$$\{c_{\boldsymbol{k},\sigma}, c^\dagger_{\boldsymbol{k}',\sigma'}\} = \delta_{\boldsymbol{k},\boldsymbol{k}'}\delta_{\sigma,\sigma'} \quad \text{and} \tag{2.29}$$

$$\{c_{\boldsymbol{k},\sigma}, c_{\boldsymbol{k}',\sigma'}\} = 0\,. \tag{2.30}$$

The Hamiltonian H_{pairing}, which describes the interaction of the electrons is given by

$$H_{\text{pairing}} = \sum_{\boldsymbol{k},\sigma} \underbrace{(\varepsilon(\boldsymbol{k}) - \mu)}_{\xi_{\boldsymbol{k}}} c^\dagger_{\boldsymbol{k},\sigma} c_{\boldsymbol{k},\sigma} + \sum_{\boldsymbol{k},\boldsymbol{k}'} \underbrace{V_{\boldsymbol{k},\boldsymbol{k}'}}_{<0} c^\dagger_{\boldsymbol{k}',\uparrow} c^\dagger_{-\boldsymbol{k}',\downarrow} c_{-\boldsymbol{k},\downarrow} c_{\boldsymbol{k},\uparrow}\,. \tag{2.31}$$

The second term prevents a complete solution of the problem, and it describes the scattering of Cooper pairs $c_{-\boldsymbol{k},\downarrow}c_{\boldsymbol{k},\uparrow}$. We expect the ground state of this system to be a phase-coherent condensate of such Cooper pairs, for which the expectation value $\langle c_{-\boldsymbol{k},\downarrow}c_{\boldsymbol{k},\uparrow}\rangle = b_{\boldsymbol{k}}$ is finite. We use a mean-field approach to solve the pairing Hamiltonian H_{pairing}. This approach is valid due to the macroscopic number of Cooper pairs in the condensate. We write the Cooper pair creation operator as

$$c_{-\boldsymbol{k},\downarrow}c_{\boldsymbol{k},\uparrow} = b_{\boldsymbol{k}} + \underbrace{(c_{-\boldsymbol{k},\downarrow}c_{\boldsymbol{k},\uparrow} - b_{\boldsymbol{k}})}_{\delta b_{\boldsymbol{k}}} \tag{2.32}$$

with the fluctuation $\delta b_{\boldsymbol{k}}$. The pairing Hamiltonian in Eq. 2.31 is now expanded up to linear order in the fluctuations, and we obtain the BCS-Hamiltonian

$$H_{\mathrm{BCS}} = \sum_{\boldsymbol{k},\sigma} \xi_{\boldsymbol{k}} c^\dagger_{\boldsymbol{k},\sigma} c_{\boldsymbol{k},\sigma} + \sum_{\boldsymbol{k},\boldsymbol{k}'} V_{\boldsymbol{k},\boldsymbol{k}'} \left(c^\dagger_{\boldsymbol{k}',\uparrow} c^\dagger_{-\boldsymbol{k}',\downarrow} b_{\boldsymbol{k}} + b^\dagger_{\boldsymbol{k}'} c_{-\boldsymbol{k},\downarrow} c_{\boldsymbol{k},\uparrow} - b^\dagger_{\boldsymbol{k}'} b_{\boldsymbol{k}} \right). \quad (2.33)$$

This Hamiltonian can be solved self-consistently with $\langle c_{-\boldsymbol{k},\downarrow} c_{\boldsymbol{k},\uparrow} \rangle = b_{\boldsymbol{k}}$. We define the superconducting gap function $\Delta_{\boldsymbol{k}}$

$$\Delta_{\boldsymbol{k}} = -\sum_{\boldsymbol{k}'} V_{\boldsymbol{k},\boldsymbol{k}'} b_{\boldsymbol{k}'} \quad (2.34)$$

and rewrite the BCS-Hamiltonian

$$H_{\mathrm{BCS}} = \sum_{\boldsymbol{k},\sigma} \left(\xi_{\boldsymbol{k}} c^\dagger_{\boldsymbol{k},\sigma} c_{\boldsymbol{k},\sigma} - \Delta_{\boldsymbol{k}} c^\dagger_{\boldsymbol{k},\uparrow} c^\dagger_{-\boldsymbol{k},\downarrow} - \Delta^*_{\boldsymbol{k}} c_{-\boldsymbol{k},\downarrow} c_{\boldsymbol{k},\uparrow} + b^*_{\boldsymbol{k}} \Delta_{\boldsymbol{k}} \right). \quad (2.35)$$

The superconducting pairing gap Δ_k always couples a state to its time reversed state.[6] This Hamiltonian can be diagonalized using a Bogoliubov-Valatin transformation. The Bogoliubov quasi-particles are defined by

$$\beta_{\boldsymbol{k},\uparrow} = u_{\boldsymbol{k}} c_{\boldsymbol{k},\uparrow} - v_{\boldsymbol{k}} c_{-\boldsymbol{k},\downarrow} \quad \text{and} \quad \beta_{\boldsymbol{k},\downarrow} = u_{\boldsymbol{k}} c_{\boldsymbol{k},\downarrow} + v_{\boldsymbol{k}} c_{-\boldsymbol{k},\uparrow}. \quad (2.36)$$

The excitation energy for Bogoliubov quasi-particles is given by

$$E_{\boldsymbol{k}} = \sqrt{\xi^2_{\boldsymbol{k}} + |\Delta_{\boldsymbol{k}}|^2} \quad (2.37)$$

with an energy gap of $|\Delta_{\boldsymbol{k}}|$ to the first excited state. The coefficients in Eq. 2.36 can be calculated to be

$$|v_{\boldsymbol{k}}|^2 = 1 - |u_{\boldsymbol{k}}|^2 = \frac{1}{2}\left(1 - \frac{\xi_{\boldsymbol{k}}}{E_{\boldsymbol{k}}}\right), \quad (2.38)$$

where the phase of one coefficient can be chosen freely and the other one is then fixed by the phase of the pairing gap. The transformation results in the Hamiltonian

$$H_{\mathrm{BCS}} = \sum_{\boldsymbol{k}} (\xi_{\boldsymbol{k}} - E_{\boldsymbol{k}} + \Delta_{\boldsymbol{k}} b^*_{\boldsymbol{k}}) + \sum_{\boldsymbol{k},\sigma} E_{\boldsymbol{k}} \beta^\dagger_{\boldsymbol{k},\sigma} \beta_{\boldsymbol{k},\sigma}, \quad (2.39)$$

where the first term is the ground state energy. The self-consistency condition yields a condition on the gap function, which can be derived from the free

[6] In the Bogoliubov-de Gennes formalism the time reversed states will be treated as hole-like particles.

energy of the system. The condition is given by

$$\Delta_{\boldsymbol{k}} = -\sum_{\boldsymbol{k}'} V_{\boldsymbol{k},\boldsymbol{k}'} \frac{\Delta^*_{\boldsymbol{k}'}}{2E_{\boldsymbol{k}'}} \tanh\left(\frac{E_{\boldsymbol{k}'}}{2k_B T}\right) . \tag{2.40}$$

In the following chapters we always assume a constant gap function as a starting point of all calculations. In the next sections we show, how superconductivity extends into normal conductors at interfaces and discuss the Bogoliubov-de Gennes formalism building on the results obtained here.

2.3.2 Superconducting proximity effect

The superconducting proximity effect occurs, when superconductors and normal conductors are brought into contact. These types of interfaces have been described by de Gennes [23] and Beenakker [24] in many possible setups. We are only concerned with the interface between a s-wave superconductor and a normal conductor. There are effects on the superconductor and the normal conductor due to the interface. We will only describe the effects in the normal conducting region.

The proximity to the superconductor opens a finite pairing gap in the normal conducting region. The magnitude of the gap is generally smaller than the gap of the proximitizing superconductor, and it decreases into the normal conducting region. The origin of this effect is the leakage of Cooper pairs into the normal conductor. The Cooper pairs can tunnel into the normal conductor and thus open a finite pairing gap due to scattering with electrons. Since this scattering has to occur coherently, the penetration depth is usually limited by the phase coherence length of the normal conductor.[7] The gap opening in the normal conducting system has the same phase as the gap in the proximitizing s-wave superconductor, because the Cooper pairs also carry the phase information of the original pairing gap.

If, instead of a normal conductor, a topological insulator is proximitized, the same process occurs. Since the bulk of the topological insulator is already gapped, the superconducting gap broadens the gap but has little effect on the bulk spectrum. However, this is not the case for the surface states. Due to the proximity effect, the surface of the topological insulator becomes superconducting and the pairing gap opens a gap at the Dirac cone. Due to the fact that only surface states are contributing, the magnitude of the pairing gap is of the

[7] Although recent experiments have shown different results [25].

same order as the original gap.

Since we want to use these proximitized topological insulator surfaces to construct Josephson junctions and networks of different junctions, we need a description of the superconducting surface Hamiltonian. In the next section we introduce the Bogoliubov-de Gennes formalism to describe superconducting systems and show how it can be used to add superconductivity to any metal or insulator model.

2.3.3 Bogoliubov-de Gennes formalism

In this section we show how we use the Bogoliubov-de Gennes formalism to describe superconducting systems. We demonstrate how the Bogoliubov-de Gennes formalism works on a simple toy model [26]. Afterwards, we explain how we use this formalism to describe superconductivity and discuss how we can treat the proximity effect for surface states easily.

The toy model, we use to describe the main features of the formalism, is a general second-quantized Hamiltonian, that may not preserve particle number. The creation and annihilation operators $c_i^\dagger$ and c_i obey fermionic commutation relations

$$\{c_i, c_j^\dagger\} = \delta_{ij} \quad \text{and} \quad \{c_i, c_j\} = 0\,, \tag{2.41}$$

and the Hamiltonian is given by

$$H_{\text{toy}} = \sum_{i,j} \left[h_{ij} c_i^\dagger c_j + \tfrac{1}{2} \left(\Delta_{ij} c_i^\dagger c_j^\dagger + \Delta_{ij}^* c_i c_j \right) \right] . \tag{2.42}$$

We collect all creation and annihilation operators in a vector and write this Hamiltonian as

$$H_{\text{toy}} = \boldsymbol{c}^\dagger h \boldsymbol{c} + \tfrac{1}{2} \left(\boldsymbol{c}^\dagger \Delta \boldsymbol{c}^\dagger + \boldsymbol{c} \Delta^\dagger \boldsymbol{c} \right) , \tag{2.43}$$

where $h = h^\dagger$ is hermitian.[8] The main idea of the Bogoliubov-de Gennes formalism is to bring the Hamiltonian into a quadratic form by doubling the

[8] We have the additional constraint $\Delta = -\Delta^T$ for the toy problem. The constraint on the pairing matrix Δ is given due to the fact, that all symmetric terms in Δ do not contribute the the Hamiltonian, because of the fermionic commutation relation. However, this is only true in this simple case, where the hole states are generated by complex conjugation alone.

degrees of freedom. We write the toy Hamiltonian as

$$H_{\text{toy}} = \tfrac{1}{2}(\boldsymbol{c}^\dagger, \boldsymbol{c}) \underbrace{\begin{pmatrix} h & \Delta \\ \Delta^\dagger & -h^T \end{pmatrix}}_{=H_{\text{BdG}}} \begin{pmatrix} \boldsymbol{c} \\ \boldsymbol{c}^\dagger \end{pmatrix} + \tfrac{1}{2}\text{tr}(h) \tag{2.44}$$

with the hermitian matrix H_{BdG}. If the original system had n degrees of freedom, H_{BdG} has the size $2n \times 2n$. Now the Bogoliubov-de Gennes Hamiltonian can be solved by a Bogoliubov-Valatin transformation, similar to the transformation described in the Bardeen-Cooper-Schrieffer theory, but this is not the focus of this section. Rather we want to emphasize the more general aspects of the Bogoliubov-de Gennes formalism.

The creation and annihilation operators are connected by time-reversal symmetry T, which is given by complex conjugation in the toy problem. Since time-reversed electrons are described as holes, the annihilation operator for an electron can be interpreted as a creation operator of a hole state. We denote the electron operators as $\boldsymbol{c}_e$ and $\boldsymbol{c}_e^\dagger$ and introduce operators $\boldsymbol{c}_h$ and $\boldsymbol{c}_h^\dagger$ as hole operators, that are related by

$$\boldsymbol{c}_h = T\boldsymbol{c}_e T^{-1} = \boldsymbol{c}_e^\dagger \,. \tag{2.45}$$

Neglecting the constant energy shift and using the fact that $T = K$, which is simply complex conjugation, and that h is Hermitian, we can rewrite Eq. (2.44) as

$$H_{\text{toy}} = \tfrac{1}{2}(\boldsymbol{c}_e^\dagger, \boldsymbol{c}_h^\dagger) \begin{pmatrix} h & \Delta \\ \Delta^\dagger & -ThT^{-1} \end{pmatrix} \begin{pmatrix} \boldsymbol{c}_e \\ \boldsymbol{c}_h \end{pmatrix} \,. \tag{2.46}$$

The operator H_{BdG} has an artificial particle-hole symmetry $\{H_{\text{BdG}}, \Xi\} = 0$ with

$$\Xi = \tau_y K \,, \tag{2.47}$$

where $\boldsymbol{\tau}$ are Pauli operators, that act on the electron-hole degree of freedom. The symmetry is there by construction and can not be broken. Therefore, it is not a symmetry in the conventional sense, since it does not commute with the Hamiltonian H_{toy}. It ensures, that the spectrum of H_{BdG} is symmetric around $E = 0$. All states with positive energy are interpreted as electron states, and all states with negative energy are interpreted as hole states. These properties of the Bogoliubov-de Gennes Hamiltonian can be used for more complicated systems to describe superconductivity.

Superconductivity in the BCS-theory originates from the finite pairing gap coupling states, that transform into each other under time-reversal. The main difference to the toy model is a more complicated time-reversal operator, since we have to account for the spin of the electrons. For $\boldsymbol{c}_e = (c_{e,\uparrow}, c_{e,\downarrow})^T$, the time-reversal operator is given by

$$T = i\sigma_y K \tag{2.48}$$

for $\boldsymbol{\sigma}$ acting on the spin degree of freedom. We again define holes as time-reversed electrons with the annihilation operator defined by

$$\boldsymbol{c}_h = T \begin{pmatrix} c_{e,\uparrow} \\ c_{e,\downarrow} \end{pmatrix} T^{-1} = \begin{pmatrix} c^\dagger_{e,\downarrow} \\ -c^\dagger_{e,\uparrow} \end{pmatrix} . \tag{2.49}$$

If we assume now a constant pairing gap Δ, we can use the the Bogoliubov formalism to write a superconducting system as

$$H_{\mathrm{SC}} = \frac{1}{2}(\boldsymbol{c}_e^\dagger, \boldsymbol{c}_h^\dagger) \begin{pmatrix} h & \Delta \\ \Delta^\dagger & -ThT^{-1} \end{pmatrix} \begin{pmatrix} \boldsymbol{c}_e \\ \boldsymbol{c}_h \end{pmatrix} , \tag{2.50}$$

where $h = h^T$ is the 2×2 Hamiltonian of the non-interacting system and Δ is a 2×2 diagonal matrix. The particle hole symmetry Ξ is here given by

$$\Xi = \sigma_y \tau_y K . \tag{2.51}$$

We will use this formalism for describing a proximitized topological insulator surface. In that case we substitute the effective surface Hamiltonian for h and fix the pairing gap to be $\Delta = \Delta e^{i\phi}$. This will be the starting point of our calculation for the topological insulator Josephson junction.

2.3.4 Andreev reflection

Andreev reflection is a process that occurs on the interface between a normal conducting and a superconducting region. We consider an electron in the normal conducting region with an energy below the magnitude of the pairing gap in the superconducting region. If it hits the interface, it has to be reflected, because its energy is below the gap of the superconductor. There are two types of reflection possible. The electron can scatter inelastically back into the normal conducting region. This process would also take place, if, instead of the superconductor, we would consider an insulator, where the energy of the incoming electron is in the band gap. The second process is Andreev reflection, which is

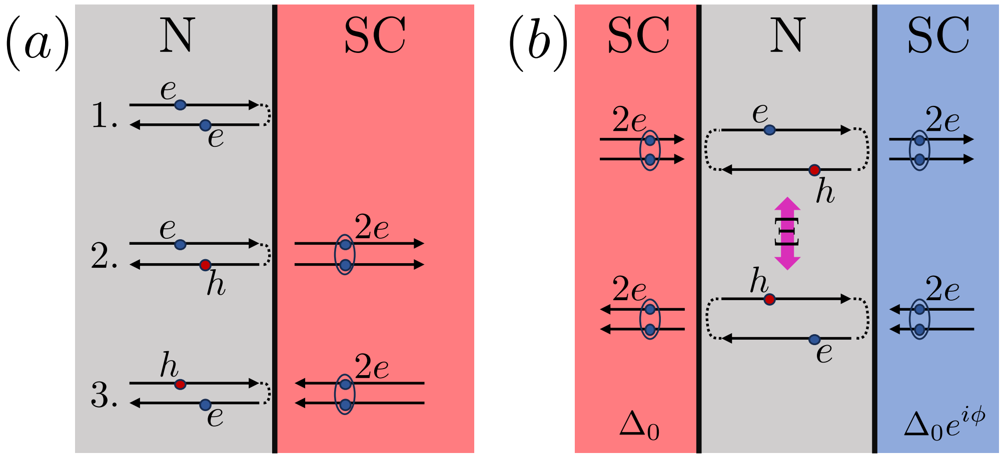

Figure 2.1: Sketch of Andreev reflection and the appearance of Andreev bound states. In (a) the three possible reflection processes on a normal conductor-superconductor (N-SC) interface are sketched: 1: normal electron to electron reflection; 2: electron to hole Andreev reflection, where a Cooper pair is absorbed in the ground state condensate; 3: hole to electron Andreev reflection, where a Cooper pair is taken from the ground state condensate. In (b) the setup for Andreev bound states is sketched. In the normal conducting region between two superconductors electrons and holes are Andreev reflected on both N-SC interfaces. If after two reflections, the state is again the initial state, an Andreev bound state appears. Each state has a partner under particle-hole transformation Ξ. Similar to a particle in a potential well, the possible energies of the bound states are quantized, and depend of the pairing gap magnitude Δ_0 and the phase difference ϕ between the superconductors.

unique to a normal conductor superconductor interface. Due to the finite pairing gap of the superconductor, the electron can be reflected into a hole state and a Cooper pair is created in the superconductor. The Cooper pair is part of the ground state condensate of the superconductor, and thus it can exist for energies below the pairing gap. The opposite process of a reflection from an incoming hole into an electron is also possible. Here, a Cooper pair is taken from the ground state condensate. All possible processes are visualized in Fig. 2.1 (a).

If we consider a setup with a normal conducting region between two superconductors, we obtain for low energies Andreev reflections on both interfaces of the junction. Now, there can be a closed loop of an electron being Andreev reflected twice into its original state. This process is sketched in Fig. 2.1 (b). Similar to an electron trapped in a potential well, there will be quantized energy levels up to the energy gap in the superconductor. Their energy depends on the phase difference between both superconductors. All Andreev bound states have a partner state, that they transform into under a particle-hole transformation. In this thesis, we will only explicitly derive Andreev bound states, that are eigenstates of the particle-hole transformation. These states always have to exist at $E = 0$, while higher energy Andreev bound states appear in pairs at $\pm E$.

Andreev bound states can be calculated in a simple way for a phase difference of π between the superconductors. If we want to treat small phase fluctuations in the superconductors perturbatively, we have to transform the problem such that the pairing gap phase is constant and the fluctuations lead to new terms in the Hamiltonian. In the next section we show, how gauge transformations of the electromagnetic field can be used to shift the phases of the pairing gap.

2.3.5 Gauge theory for superconducting systems

In this passage, we show how a gauge transformation of the electromagnetic field affects the pairing gap of a superconducting system. The section is based on de Gennes' work [27] and only gives a brief description of the consequences of gauge theory. We will not go into the early discussions, where gauge invariance was questioned in the BCS theory. For further information about this topic, we refer to work by Nambu [28] and Anderson [29]. We will only focus on the effect of a gauge field on the terms in the Bogoliubov-de Gennes Hamiltonian. This can be used later to shift the phase of the gap function onto a vector potential. The vector potential can be included via minimal coupling into the Bogoliubov-de Gennes Hamiltonian.

The electromagnetic fields can be derived from the scalar potential ϕ and the vector potential $\boldsymbol{A}$. The fields are given by

$$\boldsymbol{E} = -\boldsymbol{\nabla}\phi - \frac{\partial \boldsymbol{A}}{\partial t} \quad \text{and} \quad \boldsymbol{B} = \boldsymbol{\nabla} \times \boldsymbol{A}\,. \tag{2.52}$$

The choice of the potentials is not unique. For any potentials ϕ and $\boldsymbol{A}$ and any scalar function χ, the potentials given by

$$\phi' = \phi - \frac{\partial \chi}{\partial t} \quad \text{and} \quad \boldsymbol{A}' = \boldsymbol{A} + \boldsymbol{\nabla}\chi\,, \tag{2.53}$$

generate the same fields. The gauge field has to be real and continuous. In the bulk of a superconductor, the electric and the magnetic field have to be $\boldsymbol{E} = 0$ and $\boldsymbol{B} = 0$. One possible gauge is therefore given by

$$\phi = 0 \quad \text{and} \quad \boldsymbol{A} = 0\,. \tag{2.54}$$

However, for any time-independent gauge field $\chi(\boldsymbol{r},t) = \chi(\boldsymbol{r})$, the fields are also zero.

The choice of a gauge has to affect the pairing gap, to preserve the gauge invariance of the Bogoliubov-de Gennes Hamiltonian. The creation and annihilation operators $c^\dagger$ and c transform under a unitary operation, when applying a gauge transformation. The transformed operators are given by

$$c' = e^{ie\int^{r}\boldsymbol{A}(\boldsymbol{r'})dr'}c \quad \text{and} \quad c'^\dagger = c^\dagger e^{-ie\int^{r}\boldsymbol{A}(\boldsymbol{r'})dr'}\,. \tag{2.55}$$

For the zero-field case, the unitary transformation can be simplified to

$$e^{ie\int^{r}\boldsymbol{A}(\boldsymbol{r'})dr'} = e^{ie\chi(\boldsymbol{r})}\,. \tag{2.56}$$

Since $\Delta \propto \langle cc\rangle$, the pairing gap has to transform according to

$$\Delta' = e^{2ie\int^{r}\boldsymbol{A}(\boldsymbol{r'})dr'}\Delta = e^{2ie\chi(\boldsymbol{r})}\Delta\,. \tag{2.57}$$

Applying this to the Bogoliubov-de Gennes Hamiltonian and shifting the momentum operator $\boldsymbol{p} \rightarrow \boldsymbol{p'} = \boldsymbol{p} + e\boldsymbol{A}$ ensures the gauge invariance.[9]

If there is just one superconductor in the problem, there can also be found a gauge field such that the pairing gap is real, which can simplify calculations. If there are multiple superconductors with different phases, we can choose a gauge so we only have to consider simple phases for the superconductors. All effects of the phase variation are then shifted into the vector potential $\boldsymbol{A}$. We will use this later to treat small phase variations perturbatively.

[9]Note, that this might complicate the calculation of the time-reversed Hamiltonian, since the vector potential is not time-reversal invariant.

Chapter 3

Topological insulator Josephson junction

In this chapter, we analyze the properties of a single topological insulator Josephson junction. A Josephson junction is constructed out of two superconductors and a normal conducting or insulating barrier in between them. We are considering a setup of a linear junction on the surface of three-dimensional topological insulator. The resulting Josephson junction is effectively two-dimensional, since only surface states of the topological insulator effect the low energy regime of the junction. The details of the setup will be discussed first, and we will derive the surface Hamiltonian building on the results of Ch. 2. From the two-dimensional surface Hamiltonian, two zero-energy Majorana bound states can be derived. The calculation uses again the Jackiw-Rebbi approach, but it has to be modified slightly, due to the particle-hole symmetry of the Bogoliubov-de Gennes formalism implemented here. We will show that the Majorana modes obtained here can propagate along the junction. The propagation of the Majorana states and the gapping of the modes via the phase difference across the Josephson junction are calculated using degenerate perturbation theory. This results in an effective one-dimensional model for propagating Majorana modes, that are gapped due to time-reversal symmetry breaking. Furthermore, we consider the influence of local potential disorder on the Majorana modes and argue why higher Andreev bound states do not affect the low energy effective description. Lastly, we show that the Majorana Hamiltonian describes a one-dimensional topological model and explain why a single junction cannot be used to obtain localized Majorana edge states at the domain walls between different topological phases.

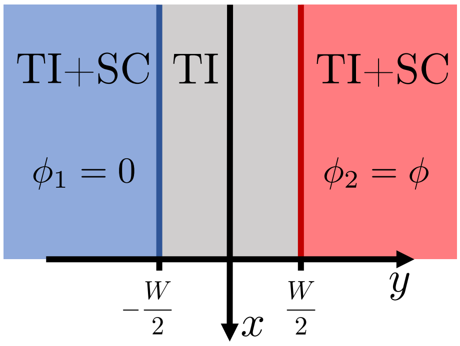

Figure 3.1: Sketch of the two-dimensional topological insulator Josephson junction. The bare topological insulator surface (TI) and with superconductor proximitized regions (TI+SC) are indicated. The phases of the pairing gap of both superconducting regions are indicated, while the magnitude of the pairing gap is Δ_0 on both sides of the junction.

3.1 Description of an infinite narrow Josephson junction

We consider an infinite narrow Josephson junction, meaning a junction of length $L = \infty$ and finite width W. The results obtained here can be used later for the finite narrow Josephson junctions in the limit $W \ll L$. As depicted in Fig. 3.1, the topological insulator surface is proximitized by two s-wave superconductors with a strip of bare surface of width W in between. The pairing gap in each superconductor takes a constant value

$$\Delta_j = \Delta_0 \, e^{i\phi_j} \tag{3.1}$$

for both sides $j = 1, 2$ of the junction. The phase of the first superconductor ϕ_1 can always be gauged to $\phi_1 = 0$, such that the phase of the second superconductor takes the value of the phase difference $\phi_2 = \phi$. The junction is extended to infinity in positive and negative x-direction to allow for free propagation along the junction. We assume the magnitude of the superconducting gap to be much smaller than the bulk gap of the topological insulator. With this approximation it is reasonable to only take the surface spectrum of the topological insulator into the description and neglect the bulk completely.

For the description of the junction we take the surface Hamiltonian in Eq. (2.28), obtained from the simplified Bernevig-Hughes-Zhang model. In the proximitized regions of the surface a superconducting gap opens, and the surfaces have to be described by the Bogoliubov-de Gennes formalism as described in Ch. 2. As a basis for the description we choose

$$\mathbf{\Psi} = \left((\psi_\uparrow^{\text{electron}}, \psi_\downarrow^{\text{electron}}), (\psi_\downarrow^{\text{hole}}, -\psi_\uparrow^{\text{hole}}) \right)^T . \tag{3.2}$$

The junction can now be modeled by varying the parameters of the superconducting gap as a function of the position on the surface. The complete Hamiltonian is given by

$$H_{\mathrm{JJ}} = \tau_z \, (v\,\boldsymbol{\sigma}\cdot\boldsymbol{p} - \mu\sigma_0) + \Delta_{\mathrm{JJ}}(\boldsymbol{r}) \, \big[\tau_x \cos\!\big(\phi_{\mathrm{JJ}}(\boldsymbol{r})\big) + \tau_y \sin\!\big(\phi_{\mathrm{JJ}}(\boldsymbol{r})\big)\big] \tag{3.3}$$

with $\boldsymbol{p} = (p_x, p_y)^T$, $\boldsymbol{r} = (x, y)^T$ and $\boldsymbol{\sigma} = (\sigma_x, \sigma_y)^T$. The $\boldsymbol{\sigma}$ are Pauli matrices acting on the spin degree of freedom, and $\boldsymbol{\tau}$ are Pauli matrices that describe the electron and hole degree of freedom of $\boldsymbol{\Psi}$. The functions describing the pairing gap are given by

$$\Delta_{\mathrm{JJ}}(\boldsymbol{r}) = \Delta_0 \, \Theta\left(|y| - \tfrac{W}{2}\right) \quad \text{and} \quad \phi_{\mathrm{JJ}}(\boldsymbol{r}) = \phi \, \Theta\left(y - \tfrac{W}{2}\right) . \tag{3.4}$$

The first term describes the Dirac surface modes separately for both electrons and holes in the Bogoliubov-de Gennes formalism. The second term captures the coupling between electrons and holes in the proximitized regions. The particle-hole symmetry operator Ξ and the time reversal operator T are given by

$$\Xi = \tau_y \sigma_y K \quad \text{and} \quad T = i\sigma_y K \, , \tag{3.5}$$

where K denotes complex conjugation. The Hamiltonian for the Josephson junction satisfies particle-hole symmetry $\{\Xi, H_{\mathrm{JJ}}\} = 0$ and is time-reversal invariant $[T, H_{\mathrm{JJ}}] = 0$ for $\phi = 0$ and $\phi = \pi$. It immediately follows from the particle-hole symmetry, that the energy spectrum is symmetric around $E = 0$.

Starting from this description of the topological insulator Josephson junction, we derive the low energy spectrum of the junction in the next section and show, how Majorana zero modes appear in the junction.

3.2 Derivation of Majorana zero modes

The calculation of the low-energy states inside the Josephson junction is similar to the derivation of the surface spectrum for the 3D topological insulator from the Bernevig-Hughes-Zhang bulk Hamiltonian in Ch. 2. We assume the phase difference across the junction being close to π. The difference $\delta\phi = \pi - \phi$ is taken into account perturbatively. We rearrange the Hamiltonian in Eq. (3.3) to obtain a generalized Jackiw-Rebbi model perpendicular to the Josephson junction

$$
\begin{aligned}
H_{\mathrm{JJ}} = & \underbrace{v\,\tau_z\sigma_y\,p_y - \mu\,\tau_z + \overbrace{\Delta_0\,\left[1 - 2\,\Theta\left(y - \tfrac{W}{2}\right)\right]}^{\Delta_{\mathrm{JR}}(y)}\tau_x}_{H_{JR}} + v\,\tau_z\sigma_x\,p_x \\
& + \Delta_0\,\left[(1-\cos(\delta\phi))\,\tau_x + \sin(\delta\phi)\,\tau_y\right]\,\Theta\left(y - \tfrac{W}{2}\right)\,.
\end{aligned} \tag{3.6}
$$

The generalized Jackiw-Rebbi Hamiltonian H_{JR} defined in Eq. (3.6) has to have two zero-energy solutions, since there are two Pauli degrees of freedom. If $H_{\mathrm{JR}}\,\xi_\pm = 0$ is rearranged to single out the partial derivative, we notice that the chemical potential enters with a different combination of Pauli matrices than the sign changing function $\Delta_{\mathrm{JR}}(y)$. We now have to solve the more complicated differential equation

$$
\partial_y \boldsymbol{\zeta}_\pm = \frac{\Delta_{\mathrm{JR}}(y)}{v}\,\tau_y\sigma_y\,\boldsymbol{\zeta}_\pm \;+\; i\,\frac{\mu}{v}\,\sigma_y\,\boldsymbol{\zeta}_\pm\,. \tag{3.7}
$$

To obtain normalizable solutions, $\boldsymbol{\zeta}_\pm$ has to be an eigenstate of the tensor product $\tau_y\sigma_y$ with eigenvalue $+1$ due to the shape of $\Delta_{\mathrm{JR}}(y)$. Since the spinor components of both terms on the right hand side commute, $[\tau_y\sigma_y, \sigma_y] = 0$, we can choose the eigenstates of $\tau_y\sigma_y$ with eigenvalue $+1$ such that they are simultaneously eigenstates of σ_y. The two normalized spinors with these properties are

$$
\boldsymbol{\eta}_\pm = (1, \pm i, \pm i, -1)^T \tag{3.8}
$$

with

$$
\tau_y\sigma_y\,\boldsymbol{\eta}_\pm = \boldsymbol{\eta}_\pm \qquad \text{and} \qquad \sigma_y\,\boldsymbol{\eta}_\pm = \pm\boldsymbol{\eta}_\pm\,. \tag{3.9}
$$

If we take $\boldsymbol{\zeta}_\pm(y) = \boldsymbol{\eta}_\pm\,f_\pm(y)$ and insert it in Eq. (3.7), it results in a differential equation for the complex scalar functions $f_\pm(y)$

$$
\partial_y f_\pm(y) = \frac{\Delta_{\mathrm{JR}}(y)}{v}\,f_\pm(y) \;\pm\; i\,\frac{\mu}{v}\,f_\pm(y)\,, \tag{3.10}
$$

which is solved by

$$
f_\pm(y) = c_\pm\, e^{\pm iy\,\mu/v + \int_0^y d\tilde{y}\,\Delta_{\mathrm{JR}}(\tilde{y})/v}\,. \tag{3.11}
$$

Thus, the two normalized solutions of the generalized Jackiw-Rebbi model are given by

$$
\boldsymbol{\zeta}_\pm(y) = \frac{1}{2\sqrt{W + v/\Delta_0}}\,(1, \pm i, \pm i, -1)^T\, e^{\pm iy\,\mu/v + \int_0^y d\tilde{y}\,\Delta_{\mathrm{JR}}(\tilde{y})/v}\,. \tag{3.12}
$$

The probability density inside the Josephson junction is constant and it decays exponentially with a decay length $\lambda_{\mathrm{SC}} = v/\Delta_0$ into both superconducting regions.

The two solutions are complex conjugates of each other and can therefore be expressed by two Majorana modes. The zero energy states can be composed into their real and imaginary part $\boldsymbol{\zeta}_\pm = \frac{1}{\sqrt{2}}(\boldsymbol{\xi}_1 \pm i\,\boldsymbol{\xi}_2)$, where each part can be viewed as a single Majorana zero mode. The two orthonormal Majorana states are given by

$$\boldsymbol{\xi}_1 = \sqrt{2}\cdot \mathrm{Re}\{\boldsymbol{\zeta}_+\} \qquad \text{and} \qquad \boldsymbol{\xi}_2 = \sqrt{2}\cdot \mathrm{Im}\{\boldsymbol{\zeta}_+\}\,. \tag{3.13}$$

Both modes are as a linear combination of $\boldsymbol{\zeta}_+$ and $\boldsymbol{\zeta}_-$ still eigenstates of the tensor product $\tau_y\sigma_y$ with the eigenvalue $+1$. Since both modes are given by real wave functions, they are also invariant under the particle-hole symmetry operator

$$\Xi\,\boldsymbol{\xi}_a = \tau_y\sigma_y K\boldsymbol{\xi}_a = \boldsymbol{\xi}_a\,. \tag{3.14}$$

This proves that the Majorana modes are their own particle-hole counterpart. Due to the particle-hole symmetry of H_{JJ}, the energy of both Majorana modes is fixed to $E = 0$.

The Majorana modes derived here are the lowest energy Andreev bound states in the Josephson junction. Energetically higher Andreev bound states can be derived for the topological insulator Josephson junction. Due to the particle-hole symmetry there must always be a pair of Andreev bound states connected by the particle-hole operator with the energies E and $-E$. The important difference to the Majorana zero modes is, that the Andreev bound states are not eigenstates of the particle-hole symmetry operator.

3.3 One-dimensional Majorana wire

The remaining terms of $H_{\mathrm{JJ}} = H_{\mathrm{JR}} + H_{\mathrm{prop}} + H_\delta$ describe the behavior of the Majorana modes propagating along the junction and the effects of a phase difference $\phi \neq \pi$ across the junction. Both effects are included perturbatively for the Majorana zero modes. The resulting effective Hamiltonian will describe a one-dimensional Majorana wire. The two perturbing terms are given by

$$H_{\text{prop}} = v\,\tau_z\sigma_x\,p_x = -v\,\tau_z\sigma_x\partial_x \overset{\text{FT}}{=} vk_x\,\tau_z\sigma_x \quad \text{and} \tag{3.15}$$

$$H_\delta = \Delta_0\,\left[\big((1-\cos(\delta\phi)\big)\,\tau_x + \sin(\delta\phi)\,\tau_y\right]\,\Theta\left(y - \tfrac{W}{2}\right)\,. \tag{3.16}$$

The energy of the Majorana modes is degenerate, and therefore we use degenerate perturbation theory to obtain an effective Hamiltonian for the low energy sector of the Josephson junction. The resulting Hamiltonian is defined by different expectation values

$$H_{\text{1D}} = \sum_{a,b=1,2} |\boldsymbol{\xi}_a\rangle\,\langle\boldsymbol{\xi}_a|(H_{\text{prop}} + H_\delta)|\boldsymbol{\xi}_b\rangle\,\langle\boldsymbol{\xi}_b|\,, \tag{3.17}$$

where the basis of this effective model is given by the two Majorana bound states.

Both perturbations will be treated separately, starting with the propagation along the junction. The momentum k_x along the junction is a good quantum number, since the translational invariance in x-direction is not broken by the junctions setup. This simplifies the calculation, because the momentum k_x can be taken out of all expectation values needed for the calculation of the effective Hamiltonian

$$\langle\boldsymbol{\xi}_a|H_{\text{prop}}|\boldsymbol{\xi}_b\rangle = k_x\,\langle\boldsymbol{\xi}_a|v\,\tau_y\sigma_y|\boldsymbol{\xi}_b\rangle\,. \tag{3.18}$$

The remaining expectation value gives the coupling of the Majorana modes to each other, and a renormalized Fermi velocity for the propagation along the junction can be obtained.

For the explicit calculation of matrix elements, we used the $\boldsymbol{\zeta}_\pm$ representation of the zero energy states. It is possible the get all the expectation values of an operator M from

$$2\,\langle\boldsymbol{\zeta}_+|M|\boldsymbol{\zeta}_+\rangle = \langle\boldsymbol{\xi}_1|M|\boldsymbol{\xi}_1\rangle + \langle\boldsymbol{\xi}_2|M|\boldsymbol{\xi}_2\rangle + i\,\langle\boldsymbol{\xi}_1|M|\boldsymbol{\xi}_2\rangle - i\,\langle\boldsymbol{\xi}_2|M|\boldsymbol{\xi}_1\rangle\,, \tag{3.19}$$

$$2\,\langle\boldsymbol{\zeta}_-|M|\boldsymbol{\zeta}_-\rangle = \langle\boldsymbol{\xi}_1|M|\boldsymbol{\xi}_1\rangle + \langle\boldsymbol{\xi}_2|M|\boldsymbol{\xi}_2\rangle - i\,\langle\boldsymbol{\xi}_1|M|\boldsymbol{\xi}_2\rangle + i\,\langle\boldsymbol{\xi}_2|M|\boldsymbol{\xi}_1\rangle\,, \tag{3.20}$$

$$2\,\langle\boldsymbol{\zeta}_-|M|\boldsymbol{\zeta}_+\rangle = \langle\boldsymbol{\xi}_1|M|\boldsymbol{\xi}_1\rangle - \langle\boldsymbol{\xi}_2|M|\boldsymbol{\xi}_2\rangle + i\,\langle\boldsymbol{\xi}_1|M|\boldsymbol{\xi}_2\rangle + i\,\langle\boldsymbol{\xi}_2|M|\boldsymbol{\xi}_1\rangle\,. \tag{3.21}$$

This simplifies the calculation for the perturbative terms. The results are

$$\langle \boldsymbol{\zeta}_+ | v\, \tau_y \sigma_y | \boldsymbol{\zeta}_+ \rangle = 0 = \langle \boldsymbol{\zeta}_- | v\, \tau_y \sigma_y | \boldsymbol{\zeta}_- \rangle \quad \text{and} \tag{3.22}$$

$$\langle \boldsymbol{\zeta}_- | v\, \tau_y \sigma_y | \boldsymbol{\zeta}_+ \rangle = iv \frac{\Delta_0^2}{\Delta_0^2 + \mu^2} \frac{\cos\left(\frac{\mu W}{v}\right) + \frac{\Delta_0}{\mu} \sin\left(\frac{\mu W}{v}\right)}{\frac{W\Delta_0}{v} + 1} = i\tilde{v} \tag{3.23}$$

and from that the momentum-dependent part of the effective Hamiltonian follows to

$$\sum_{a,b=1,2} |\boldsymbol{\xi}_a\rangle\, \langle \boldsymbol{\xi}_a | H_{\mathrm{prop}} | \boldsymbol{\xi}_b \rangle\, \langle \boldsymbol{\xi}_b | = \tilde{v} k_x\, \tilde{\sigma}_x \,. \tag{3.24}$$

This part of the effective Hamiltonian yields a one-dimensional Dirac spectrum, where $\tilde{\boldsymbol{\sigma}}$ act on the basis of the two Majorana zero modes $\boldsymbol{\xi}(x) = (\xi_1(x), \xi_2(x))^T$.

To include deviations from a phase difference of $\phi = \pi$, we use a gauge transformation $\chi(y)$. With this transformation the phase of the superconducting gap function for $\frac{W}{2} < y$ is fixed to $\phi = \pi$. Simultaneously, we do not want to affect the gap function for $y < -\frac{W}{2}$, and the gauge has to be chosen continuous. The simplest solution that fulfills these conditions is

$$\chi = \begin{cases} 0 & y < -\frac{W}{2} \,, \\ \frac{\delta\phi}{2eW} \left(y + \frac{W}{2}\right) & |y| < \frac{W}{2} \,, \\ \frac{\delta\phi}{2e} & \frac{W}{2} < y \,. \end{cases} \tag{3.25}$$

This gauge results in a non-zero vector potential $\boldsymbol{A}$ inside the Josephson junction

$$\boldsymbol{A} = \frac{\delta\phi}{2eW}\, \Theta(\tfrac{W}{2} - |y|)\, \boldsymbol{e}_y \,, \tag{3.26}$$

that acts therefore only on a finite region in y-direction. Since the Dirac dispersion of the surface states of the topological insulator is linear in $\boldsymbol{p}$, the vector potential can be included easily via minimal coupling. The junction is now considered at a phase difference, where time reversal invariance is broken. Instead of H_δ we now consider

$$H_{\boldsymbol{A}} = \frac{v\, \delta\phi}{2W} \boldsymbol{e}_y \cdot \boldsymbol{\sigma} = \frac{v\, \delta\phi}{2W}\, \sigma_y \tag{3.27}$$

as perturbation due to finite ε. We only take perturbations up to first order in ε into account. Still we need all possible matrix elements between the two Majorana zero modes and calculate them again in the $\boldsymbol{\zeta}_\pm$ basis. The results are given by

$$\langle \boldsymbol{\zeta}_+ | \tfrac{v\,\delta\phi}{2W}\,\sigma_y | \boldsymbol{\zeta}_+ \rangle = -\,\langle \boldsymbol{\zeta}_- | \tfrac{v\,\delta\phi}{2W}\,\sigma_y | \boldsymbol{\zeta}_- \rangle = \frac{\delta\phi\Delta_0}{2}\,\frac{1}{\frac{W\Delta_0}{v}+1} = \delta \quad \text{and} \tag{3.28}$$

$$\langle \boldsymbol{\zeta}_- | \tfrac{v\,\varepsilon}{2W}\,\sigma_y | \boldsymbol{\zeta}_+ \rangle = 0\,. \tag{3.29}$$

From these expectation values we calculate the contribution of the gauge field to H_{1D} and it enters as the mass term

$$\sum_{a,b=1,2} |\boldsymbol{\xi}_a\rangle\ \langle \boldsymbol{\xi}_a | H_{\boldsymbol{A}} | \boldsymbol{\xi}_b \rangle\ \langle \boldsymbol{\xi}_b | = \delta\,\tilde{\sigma}_y \tag{3.30}$$

into the one-dimensional Hamiltonian. The mass can be tuned by varying the phase difference across the Josephson junction.

The full effective Hamiltonian describing the one-dimensional Majorana wire is given by

$$H_{\mathrm{1D}} = \tilde{v}k_x\tilde{\sigma}_x + \delta\tilde{\sigma}_y\,. \tag{3.31}$$

The Pauli operators $\tilde{\boldsymbol{\sigma}}$ act on the basis $\boldsymbol{\xi}(x) = (\xi_1(x), \xi_2(x))^T$. The $\xi_a(x)$ are Majorana modes corresponding to the two zero energy bound states in the Josephson junction. Both modes are a equal mixture of all spin, orbital and particle-hole states in the full three dimensional description, and this structure can be derived from all dimension reducing transformations. In this low-energy description this is all captured in the two modes $\xi_a(x)$. For this basis the particle-hole and time-reversal symmetry operators are

$$\Xi = K \quad \text{and} \quad T = i\tilde{\sigma}_y K\,. \tag{3.32}$$

The particle-hole symmetry of the Hamiltonian of the Josephson junction is preserved. For finite δ the effective Hamiltonian is not time reversal invariant, which is consistent with the full H_{JJ}. The spectrum E_k of H_{1D} is

$$E_k = \pm\sqrt{(\tilde{v}k_x)^2 + \delta^2}\,. \tag{3.33}$$

This spectrum can be compared to the spectrum for a junction with $W = 0$ and $\mu = 0$ derived by Fu and Kane [7]. They obtained

$$E_{\mathrm{ideal}} = \pm\sqrt{(vk_x)^2 + \Delta_0 \cos\left(\frac{\phi}{2}\right)} \tag{3.34}$$

for $\phi = \pi - \delta\phi$. In this limit we obtain $\tilde{v} = v$ and $\delta = \frac{\delta\phi\Delta_0}{2}$, which is consistent with their result. We use their more general result for an estimation of the mass term δ in the cases, where we have a phase differences across a Josephson junction, which cannot be approximated with our perturbative result. As we show later, the exact value of δ is not as important as the sign of the mass term.

3.4 Effects of disorder on the effective Hamiltonian

We specify two different types of disorder for the topological insulator Josephson junction in the two dimensional system. The first kind of disorder V preserves the particle-hole symmetry Ξ of the system

$$\{V, \Xi\} = 0 \,. \tag{3.35}$$

Disorder in the chemical potential $V = V(\boldsymbol{r})\,\tau_z$ fulfills the condition in Eq (3.35). The second type of disorder is not particle-hole symmetry preserving. One possible source of a term like this are magnetic fields, that have the form $\boldsymbol{B}(\boldsymbol{r}) \cdot \boldsymbol{\sigma}$ in our basis.

For the symmetry-preserving disorder we first consider the effects of the disorder on the one-dimensional effective Hamiltonian. The disorder is taken into account perturbatively. Concerning all expectation values needed for the degenerate perturbation approach, we obtain

$$\langle \boldsymbol{\xi}_a | V | \boldsymbol{\xi}_b \rangle = \langle \boldsymbol{\xi}_a | \Xi^{-1} (\Xi V \Xi^{-1}) \Xi | \boldsymbol{\xi}_b \rangle = - \langle \boldsymbol{\xi}_a | V | \boldsymbol{\xi}_b \rangle \,, \tag{3.36}$$

and from this follows

$$\langle \boldsymbol{\xi}_a | V | \boldsymbol{\xi}_b \rangle = 0 \,. \tag{3.37}$$

Any symmetry-preserving perturbation to the system does not affect the low-energy one-dimensional effective Hamiltonian. The Majorana modes are protected by particle-hole symmetry and therefore they are not perturbed by any symmetry preserving term. Accordingly the Majorana modes can not interact with any fully localized states, that appear for stronger disorder. Even though, these localized states can have energies arbitrarily close to the propagating Majorana modes, H_{1D} is not affected by their presence.

Secondly, we consider the effects of disorder on higher Andreev bound states. These states are not protected by particle-hole symmetry and therefore perturbed by the disorder in the system. For sufficiently high disorder, the scattering due to the disorder potential results in a phase coherence length $l_{\text{coh}} < W$ of the proximitized surface, and no Andreev bound states are possible. The decoherence of the scattered electrons and holes prohibits the phase coherent superposition of electron and hole states, which is needed for Andreev bound states. Of all propagating states, only the Majorana modes survive in the Josephson junction, because they are the only ones, that have to appear in the junction, which was shown with the generalized Jackiw-Rebbi model. The low energy effective model becomes even more valid in this case, since the energy gap from the transversal Majorana zero modes to the energetically next highest propagating state in the system is larger.

The second type of disorder is only relevant for Josephson junctions with finite width. If $W = 0$, the presence of the finite superconducting gap function enforces particle-hole symmetry on the full surface of the topological insulator.[1] In general, for finite W, the particle-hole symmetry-breaking perturbation affects the low energy effective Hamiltonian. For weak disorder, it can introduce additional terms into H_{1D}, which gap out the spectrum for the case $\delta = 0$. Even for the weakly perturbed system, the symmetry protection of the Majorana modes is lifted. If the symmetry protection of the Majorana modes is broken, particle-hole symmetric perturbations of the first disorder type affect the low energy spectrum of the Josephson junction. Especially the strong local potential disorder, that was considered before, can now destroy the Majorana bound states as well as the higher order Andreev bound states.

In the following, we always assume that there is strong enough particle-hole symmetric disorder in the Josephson junction to destroy higher Andreev bound states. Furthermore, we only consider the situation, that there are no perturbations in the system, which are not particle-hole symmetric. The second assumption is valid in the narrow junction limit, since there the superconductivity ensures the particle-hole symmetry of the system due to the proximity effect. In this case, the low energy one dimensional effective model is valid.

[1] This situation can be achieved for systems, where W is smaller than the effective surface coherence length of the proximitized topological insulator surface. Then the proximitized regions extend so far, that they meet and the effective width of the Josephson junction is $W = 0$.

3.5 Topology of the Majorana wire

To create the Majorana lattice in Ch. 5 we need localized Majorana modes on the lattice sites and wires, which connect lattice sites, to obtain interaction. As we will show later, the topological insulator Josephson junction can be used as such a wire to bring forth interactions between localized Majorana bound states. We still need to obtain localized Majorana modes to create the lattice and we can use the topological properties of the Majorana wire to find such modes.

If we just assume, that we can influence the parameter δ in the Majorana wire Hamiltonian $H_{1\mathrm{D}}$ defined by Eq. (3.31), we can construct a situation where

$$\delta(x) = \begin{cases} \delta_1 > 0 & x > 0 \\ \delta_2 < 0 & x < 0 \end{cases} . \tag{3.38}$$

Then $H_{1\mathrm{D}}$ is a Jackiw-Rebbi Hamiltonian, now defined for Majorana modes instead of fermionic modes as before. Therefore, we obtain a localized state at $x = 0$, where the sign of δ changes. Using this, we can define two topological phases of the Majorana wire with the sign of δ as topological invariant, since the Jackiw-Rebbi model only yields edge states between different topological phases. It is clear that the phase transition occurs at $\delta = 0$.

In the next chapter, we will build on this topological property of the Majorana wire to obtain Majorana bound states. However, we always have to keep in mind, that the Majorana wire is the low energy description of a topological insulator Josephson junction. If we want to build a network of Majorana wires, we have to account for the superconducting regions of the topological insulator surface. There are situations, where the constraint, that the pairing gap phases in continuous superconductors must be constant, does not allow for a specific tuning of the Majorana network. This is also the reason why we need three independent superconducting regions, as we will show in the next chapter.

Chapter 4

Localized Majorana state

In this chapter, we want to obtain a localized Majorana bound state on the topological insulator surface. We need these states to construct the hexagonal lattice. In the last section of the previous chapter, we showed, that the low-energy regime of a topological insulator Josephson junction corresponds to a topological Majorana wire. We identified the two phases of this one-dimensional model. Our approach of finding a Majorana bound state is based on the idea of introducing a domain wall between two different topological regimes. At this domain wall, we expect a localized boundary state. However, there is one problem with this approach. We need at least three different superconductors to realize the phase differences across the junctions for two distinct domains in the Majorana wire. If the phases are tuned to achieve a wire with two domains, there must be a third Josephson junction. In this chapter, we will describe how these trijunction setups can be treated and show that the naive approach of finding a localized Majorana bound state at a domain wall leads to a general result for trijunctions. We will be able to obtain a phase diagram for the appearance of Majorana bound states in the junction, which can be compared to results derived in different limits. We will also show, that Majorana bound states exist in a trijunction with identical absolute value of the phase difference across each junction and a discrete rotational invariance of $2\pi/3$. Out of these junctions, we will be able to construct the hexagonal Majorana lattice.

4.1 Localized Majorana state at domain wall

We want to obtain a localized Majorana bound state starting from the topological Majorana wire described by $H_{1\text{D}}$ in Eq. (3.31). We consider the narrow junction limit and expand $\tilde{v}$ and δ to zeroth order in $W\Delta_0/v$. This can be motivated with the extension of the proximitized region into the physical gap

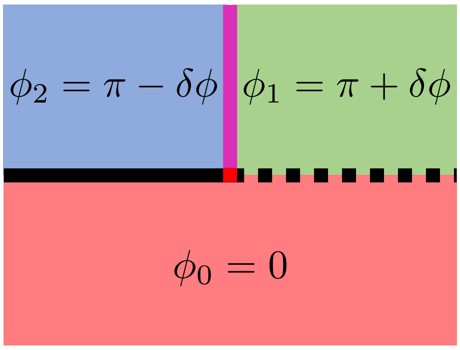

Figure 4.1: Sketch of a topological insulator Josephson junction with a topological domain wall (red dot). The Majorana wire (black line) has two topological phases, represented by the solid and dashed line. Where the two phases meet, a domain wall is present. If the phases of the proximitizing superconductor ϕ_i are chosen such that a topological domain wall is created in the Majorana wire, an additional Josephson junction (pink line) appears.

between the superconductors. Further we set $\mu = 0$ and the parameters of the wire are given by

$$\tilde{v} = v \quad \text{and} \quad \delta = \delta\phi \tfrac{\Delta_0}{2} \,. \tag{4.1}$$

To realize a domain wall, the parameter δ has to change sign once along the wire. The simplest choice of the superconducting phases to create such a wall is shown in Fig. 4.1, but it is clear from the sketch, that we cannot obtain a topological domain wall without creating a third Josephson junction. We only consider the symmetric tuning of the phases in this section as depicted in Fig. 4.1. For all $\varepsilon \neq 0$ the third Josephson junction must exist and host propagating Majorana modes with energies below the magnitude of the pairing gap in the topological insulator surface Δ_0. If we only consider $\delta\phi \ll 1$, the gap in the new junction δ_{new} is far larger than the gap in the junction, where we want to create the domain wall. According to [7, 30] the gap in the new Josephson junction must be of the order of Δ_0 with quadratic corrections in $\delta\phi$.[1] If $\delta_{\text{new}} = \Delta_0 + \mathcal{O}(\delta\phi^2)$, we do not have to take the new junction into account for the low-energy description of the junction with the domain wall. The reason for this is, that the gap between the low-energy states in the junction with domain wall and the excited states in the proximitized regions are of the same order. Therefore they are neglected in the low-energy expansion. The existence of the third junction is only important to allow the phase tuning needed for a domain wall, but can otherwise be neglected. Later, we show that this is not true in general and that there are situations where all junctions contribute identically.

With this simplification, we can describe the problem now with a one-dimensional

[1]There would also be corrections due to a finite width W of the third junction, but these are neglected in the idealized limit we consider here. If for all junctions the finite width would be treated identically, the results presented here would not change, if all junctions have the same size.

Hamiltonian

$$H_{\text{domain wall}} = -iv\tilde{\sigma}_x\partial_x + \delta(x)\tilde{\sigma}_y\,, \tag{4.2}$$

where the $\tilde{\boldsymbol{\sigma}}$ act on the Majorana basis $(\xi_1(x), \xi_2(x))^T$ and with the position dependent gap

$$\delta(x) = \begin{cases} \frac{\delta\phi\Delta_0}{2}\,, & x < 0 \\ -\frac{\delta\phi\Delta_0}{2}\,, & x > 0 \end{cases}\,. \tag{4.3}$$

Depending on the sign of $\delta\phi$, the signs of both cases of $\delta(x)$ for $x \gtrless 0$ change. This change of sign corresponds to a topological phase transition of both domains of the Majorana wire, and for the symmetric choice of $\delta\phi$, this transition happens in both domains simultaneously. Therefore, we always have a domain wall at $x = 0$. This model is now a Jackiw-Rebbi model for two Majorana modes. We formulated the Jackiw-Rebbi model in Ch. 2 for a general basis, so we can take all results from this chapter to calculate the boundary state at the domain wall. Since we only have two Majorana modes contributing and therefore have one Pauli degree of freedom, we obtain a single Majorana bound state. Therefore, a single Majorana mode is localized at the domain wall, and its energy is fixed to $E = 0$, which is always true for the localized solution of a Jackiw-Rebbi model. The Majorana bound state is given by

$$\boldsymbol{\xi}_{\text{MBS}} = \boldsymbol{\chi}(\delta\phi)\, e^{-\Delta_0|x|\,|\delta\phi|/2} \tag{4.4}$$

with

$$\boldsymbol{\chi}(\delta\phi) = \begin{cases} (0,1)^T\,, & \delta\phi < 0 \\ (1,0)^T\,, & \delta\phi > 0 \end{cases}\,. \tag{4.5}$$

Depending on $\delta\phi$, the Majorana mode, which gives the bound state, changes, but this can only occur at the phase transition of the wire.

A Majorana bound state is obtained by neglecting one of the junctions completely. In the next section, we describe how variations of the phases affect the Majorana bound state. There, we will show that the results from the approach given here can be generalized to arbitrary phases of the superconducting surface regions.

4.2 Phase variations

In this section, we want to show how the Majorana bound state behaves, if the phases of the three superconductors are tuned independently of each other. We

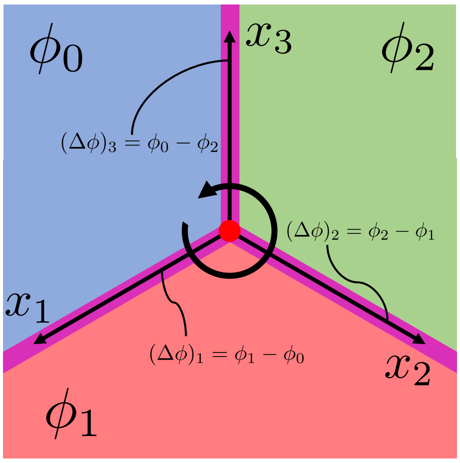

Figure 4.2: Sketch of a Josephson trijunction with $2\pi/3$ rotational symmetry. Three half-infinite topological insulator Josephson junctions (pink lines) meet in a trijunction (red dot). The angle between them is $2\pi/3$. For each individual junction the coordinates $x_i \geq 0$ are sketched for $i = 1, 2, 3$ with $x_i = 0$ at the trijunction. The phase differences $(\Delta\phi)_i$ for each Majorana wire between the superconducting regions are measured counter-clockwise around the trijunction, indicated by the curved arrow. Each junction is described by the one-dimensional Majorana wire Hamiltonian derived in the previous chapter with $(\Delta\phi)_i$ as phase difference across the Josephson junction.

will treat this in a $2\pi/3$ rotational invariant setup, because we have to treat less distinct cases to obtain results for arbitrary phases and since this is the element from which we will construct the hexagonal Majorana lattice. For this setup, we will identify two distinct situations, one with a localized Majorana bound state and one without. We will show, how tuning the phases effects both cases and how the transition between them can be explained.

We take the setup from the previous section and deform the superconducting regions, we obtain junctions which meet at a rotational symmetric trijunction. From now on, we will speak of three half-infinite Josephson junctions, which meet in one point. Each junction has its own coordinate $x_i \in [0, \infty]$ with $i = 1, 2, 3$, where $x_i = 0$ describes the trijunction. The phase difference across each junction has to be measured now clockwise around the trijunction, to get the right parameters for each junction. In Fig. 4.2 this symmetric trijunction is sketched, and the coordinates for each Josephson junction are shown. Each junction can be described as an individual half-infinite topological Majorana wire with the Hamiltonian

$$H_i = -iv\tilde{\sigma}_x\partial_{x_i} + \delta_i\tilde{\sigma}_y \quad \text{with} \quad x_i > 0\,. \tag{4.6}$$

Instead of describing the problem as a general scattering problem between the three junctions, we identify two special cases, that can be generalized using the topological properties of each junction.

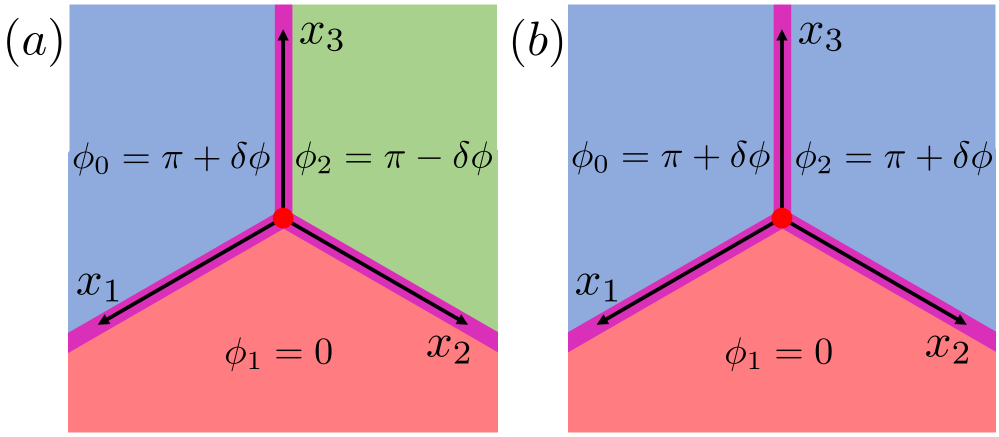

Figure 4.3: Sketch of a trijunction of three half-infinite topological insulator Josephson junctions for differently tuned phase setups. In both cases, the gap δ_3 is of the order of the superconducting pairing gap in the proximitized regions, and the third junction can be neglected in the low-energy description of the trijunction. In (a) the superconducting phases are tuned, such that the trijunction hosts one localized Majorana state. In (b) the junction will not host a Majorana bound state.

We consider two differently tuned phase setups, from which the first is identical to the situation before and the second could be realized with two superconductors without a third junction. Both setups are sketched in Fig. 4.3. In both cases the third junction can be neglected for the low-energy description, since the gap here is similar to Δ_0. We define a coordinate x along the contributing junctions 1 and 2 as

$$x = \begin{cases} -x_1\,, & x < 0 \\ x_2\,, & x > 0 \end{cases}. \tag{4.7}$$

After the coordinate transformation, the total Hamiltonian takes the form

$$H_{\text{trijunction}} = -iv\tilde{\sigma}_x\partial_x + \delta(x)\tilde{\sigma}_y \tag{4.8}$$

with

$$\delta(x) = \begin{cases} -\delta_1\,, & x < 0 \\ \delta_2\,, & x > 0 \end{cases}. \tag{4.9}$$

Now, we consider both phase setups individually. If the phases are tuned as shown in Fig. 4.3 (a), we obtain

$$\delta_1 = \delta_2 = \delta\phi\,\tfrac{\Delta_0}{2}\,. \tag{4.10}$$

This leads to a sign change in $\delta(x)$ after the transformation, and therefore to a domain wall in the low-energy model for the trijunction. Depending on the sign of $\delta\phi$, the spinor structure of the Majorana mode changes according to Eq. (4.5). This setup will always host a Majorana bound state in the trijunction. For the situation shown in Fig. 4.3 (b), the gaps in the two contributing junctions already have a different sign

$$\delta_1 = -\delta_2 = \delta\phi \, \tfrac{\Delta_0}{2} \, . \tag{4.11}$$

After the transformation $\delta(x) = -\delta_1$ is constant. Therefore, there will not be a Majorana bound state localized at the trijunction. For both phase setups, this fulfills the expectations, since the first setup is very similar to the situation in the previous section and the second setup resembles one junction with a kink but no domain wall.

For the phase setup, where a Majorana mode is localized in the trijunction, we vary the phases of the superconductors continuously without ever having a phase difference of $\Delta\phi = \pi$ across a junction. If there never is a phase difference of $\Delta\phi = \pi$ across any junction, all junctions are always gapped and the zero energy Majorana mode has to stay at the junction. Phase variations like this define topological equivalence classes, because they transform the Hamiltonian without ever closing the energy gap. If we tune one phase difference exactly to $\Delta\phi = \pi$, one Majorana wire becomes gapless and the Majorana mode becomes part of the spectrum of that junction. When we tune this Josephson junction away from the gapless point, two things can happen. If we reverse the phase variation, which brought us to the gapless point, we will again create a Majorana mode at the trijunction, since the situation is topologically equivalent to the setup in the beginning. But if we tune the phase such that we do not reverse previous variations, we end up in a setup, which is topologically equivalent to the phase setup in Fig. 4.3 (b), and does not host a Majorana bound state. The topological phase transition of one topological insulator Josephson junction results in a phase transition between the two topologically different phase setups.

We have shown, that the appearance of a Majorana bound state is tied to the two topologically different phase setups of the trijunction. The appearance of Majorana zero modes is therefore not a result of fine tuning of the pairing gap phases, but a topological property of the trijunction. However, there are effects of the exact phases of the pairing gap in the three proximitized regions.

Depending on each phase difference, the expansion of the zero-energy state into the individual Josephson junctions varies, but the mode has to stay localized. The smaller the gap δ_i of each Majorana wire is, the farther the localized mode extends into this wire. We have to keep this in mind, when we want to construct the hexagonal lattice out of individual trijunctions in Ch. 5.

Before we introduce the lattice of Majorana bound states, we will derive a diagram of the topological phases depending on the superconducting phases in the next section. We will use this later to obtain a lattice with Majorana bound states at every trijunction and we will compare our results to a different approach of treating the trijunction as a three-terminal Josephson junction.

4.3 Phase diagram

In this section, we will derive a diagram of the two topological phases of the trijunction, depending on the phases of the pairing gap. With this diagram, we will show, how the topological phase of a trijunction is easily determined from the pairing gap phases. To construct a diagram of the topological phases, we assume one of the pairing gaps has the phase $\phi_0 = 0$. Then, we only have to vary the other two superconducting phases ϕ_1 and ϕ_2. From the derivation above, we know, that there is a topological phase transition of the trijunction, if and only if one of the Majorana wires undergoes a phase transition. This happens if one phase difference between the three superconducting regions is exactly $\Delta\phi_{ji} = \pi$. This results in three conditions for a phase transition, which are given by

$$\phi_1 = \pi \quad \text{or} \quad \phi_2 = \pi \quad \text{or} \quad \phi_1 - \phi_2 = \pm\pi \,. \tag{4.12}$$

If any of these conditions is fulfilled, the junction undergoes a phase transition. If we draw the lines corresponding to the phase transitions in a ϕ_1-ϕ_2-diagram, we split the diagram into three areas.[2] The phase transition lines are shown in Fig. 4.4. For each area, we know from the previous section, whether the trijunction hosts a localized Majorana mode or not, since the special cases discussed lie in different areas.[3] Since all points in one area connected by continuous phase variations, which do not close any gap, each area belongs to the same topological equivalence class. The difference between the two regions, where a

[2] Keep the periodicity of ϕ_i in mind and associate a phase of 2π with 0.

[3] Since we never specified whether $\delta\phi$ is positive or negative, we have a special case in each triangular area. For the trivial case, the sign of $\delta\phi$ does not matter, because both cases are connected by continuous phase variations, which never close a gap.

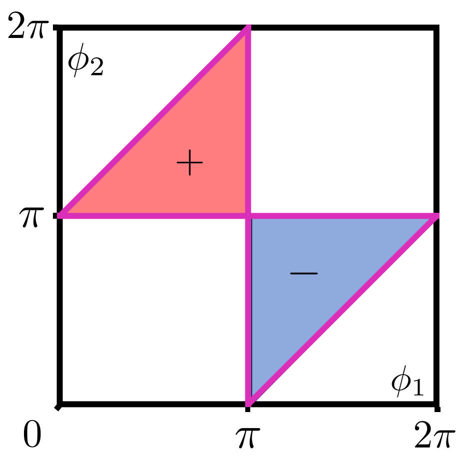

Figure 4.4: Diagram of the topological phases of the trijunction of topological insulator Josephson junctions. Assume $\phi_0 = 0$ and tune the other two pairing gap phases to arbitrary values. The trijunction will be in a topological phase and host a Majorana bound state, if the point in phase space is in the colored areas. For each color the spinor structure of the Majorana bound state is different. The labeling with $\pm$ is given by the discrete vorticity of the phases around the junction. The pink lines indicate the topological phase transitions.

Majorana mode is present, is the spinor structure of the mode.

Another way to visualize the different phases is to plot $e^{i\phi_j}$ for $j = 0, 1, 2$ on the unit circle in the complex plane and connect the three points in the order of j. According to Fig. 4.4, if the origin is inside the triangle, a Majorana bound state is located at the trijunction. The spinor structure of the Majorana mode can be associated with the direction in which the lines go around the origin. If the origin is outside the triangle, no Majorana bound state is present. The three situations are sketched in Fig. 4.5. This figure shows the discrete vorticity ν of the three pairing gap phases, which can be calculated by

$$\nu = \frac{1}{2\pi i} \oint_\Gamma \frac{1}{z} dz \,, \tag{4.13}$$

where Γ is the closed path one gets when connecting $e^{i\phi_j}$. The integration goes along the edge of the triangle in Fig. 4.5. The right orientation of the closed curve is given by the measurement of the pairing gap phases counter-clockwise around the trijunction. For three superconducting regions, the phase can wind only once around the origin counter-clockwise or clockwise, which corresponds to a vorticity of $\nu = \pm 1$, or not at all, which results in $\nu = 0$. The vorticity immediately shows, if there is a Majorana bound state at the trijunction. For $\nu \neq 0$, there must be a Majorana bound state and the sign of ν also gives the spinor structure of the Majorana mode. Since the sign of ν distinguishes between the two different spinor structures, we use it to denote the two different Majorana modes. For three arbitrary phases, we only have to calculate the discrete vorticity of the pairing gap phases to know the topological phase of the trijunction.

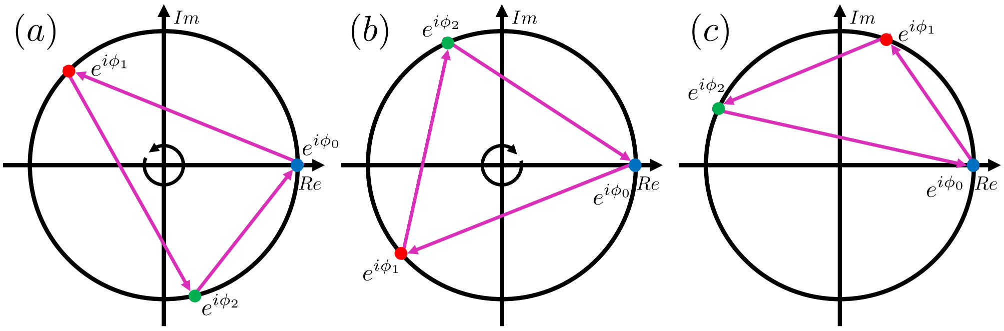

Figure 4.5: Visualization of discrete vorticity of the superconducting phases in connection with the appearance of Majorana bound states. For the three topological phases of the trijunction, the three pairing gap phases are shown on the unit circle in the complex plane. The arrows (pink) connect the points, when measuring the pairing gap phases in the counter-clockwise direction around the trijunction. If the origin is inside the triangle, which the arrows form, the path winds around the origin, indicated by the curved arrow. The discrete vorticity will be non-zero, and the trijunction will host a Majorana mode. In (a), the path along the arrows surrounds the origin in counter-clockwise direction and the discrete vorticity is $+1$. In (b), the path along the arrows surrounds the origin in clockwise direction and the discrete vorticity is -1. In (c), the path does not wind around the origin, and there will be no Majorana bound state.

Our result agrees with work done by van Heck *et al.* in [31], where they analyzed a general scattering region connecting three different superconductors. In this three-terminal Josephson junction, the superconductors are separated, and scattering between them leads to the appearance of Majorana zero modes. Their topological phase diagram for the scattering with disordered configurations agrees completely with Fig. 4.4. We want to emphasize, that we obtained the connection between the topological phases and the discrete vorticity ν as a result of the analysis of the trijunction. For a continuous p-wave superconductor and a continuous vortex originating from a magnetic flux, a Majorana bound state is localized at the vortex according to [32]. However, it was not clear from the beginning, that the junction has to host a Majorana bound state for a discrete vortex, since there we have the three Josephson junctions as gaps between the superconductors.

We now have a condition for Majorana zero modes to be localized at a trijunction. In the next chapter, we will construct a Majorana lattice out of trijunctions connected by narrow topological insulator Josephson junctions. We will show, how we can tune the phases of the hexagonal superconducting regions to create non-zero discrete vorticity at every trijunction, which will lead to a hexagonal lattice of Majorana bound states. The analysis of this lattice will be the main topic of the next chapter.

Chapter 5

Hexagonal Majorana fermion lattice

In this chapter, we construct a lattice of Majorana fermions and analyze its transport properties. For the construction of the lattice we use the trijunctions discussed in the previous chapter and connect them with narrow topological insulator Josephson junctions. The resulting network is hexagonal, and for each hexagon the phase of the pairing gap has to be fixed. We will show, that there are tilings of the pairing gap phases, where each trijunction hosts a Majorana fermion. Further, we will show, that there is a special tiling, where the wave function of the Majorana bound state extends equally far into every Josephson junction. This leads to a regular lattice with two trijunctions with different vorticity in each unit cell. Since the Josephson junctions between different trijunctions are not infinite, the wave functions of neighboring Majorana fermions will overlap, which leads to an interaction between the Majorana modes localized at different trijunctions. Due to the fact that the wave functions decay exponentially in the Josephson junctions, this interaction will be weak and strongly dependent on the distance a between the trijunctions. The weak interaction of neighboring Majorana fermions, which are otherwise localized at each junction, justifies a tight-binding description of the hexagonal Majorana lattice. We calculate the spectrum of the Majorana lattice from the resulting tight-binding Hamiltonian and compare it to the spectrum of graphene. Furthermore we want to analyze the transport properties of the Majorana lattice. For this we will use a library called Kwant [33], but this library is written for transport problems of standard fermions. To solve this issue, we introduce a transformation of the hexagonal Majorana lattice to a diamond-shaped lattice of spinless fermions with a finite superconducting pairing gap. For the fermionic lattice we can now use built-in functions of the library to show different transport properties. Since the Majorana fermions do not carry electrical charge, we are interested only in thermal transport. We will derive the one-dimensional transport spectrum for a ribbon geometry for open and for periodic boundary conditions, where we obtain edge states for the open boundaries. Moreover, we analyze the scaling of the conductance G depending on the ratio of the dimensions of the Majorana lattice. We will show, how $G \times L/W$ approaches a constant value in the short-wide junction limit. In the last section of this chapter, we will introduce disorder into the Majorana lattice. In the derivation of the tight-binding Hamiltonian we will show that the parameters of the Majorana lattice strongly depend on the phases of the pairing gaps. If there are phase fluctuations present, this will lead to a disordered hopping between the Majorana fermions. We will analyze the transport properties of the hexagonal Majorana lattice in the presence of disordered hopping, and analyze the scaling behavior of this lattice numerically.

5.1 Description of the hexagonal Majorana lattice

The construction of the hexagonal lattice is simple, if we take the $2\pi/3$ rotational-symmetric trijunctions and connect them with Majorana wires. If each wire has the same length a, we will obtain a hexagonal network of Majorana wires. This can be realized by placing hexagonal superconducting regions on the surface of a topological insulator. If the edges of neighboring superconducting regions are parallel to each other, there will be a topological insulator Josephson junction between each hexagon. To end up with the Majorana wire network, we have to take the effective low energy description of each Josephson junction. The setup is sketched in Fig. 5.1, and it is indicated there, how this system realizes the Majorana wire network.

Each superconducting hexagon has to have a constant pairing gap phase, and we have to find a tiling of the phases, which results in a Majorana fermion at each trijunction to obtain the hexagonal Majorana lattice. We consider a situation with three different superconducting phases ϕ_j with $j = 0, 1, 2$. If these three phases result in a non-zero discrete vorticity at a trijunction, we know that a Majorana bound state must exist at the trijunction. Now we only have to ensure, that for each trijunction all three phases are present. This is equivalent to the condition, that neighboring hexagons never have the same phase. Mathematically, this corresponds to the tiling problem of an infinite hexagonal lattice with three colors. The proof is intuitively clear and can be proven rigor-

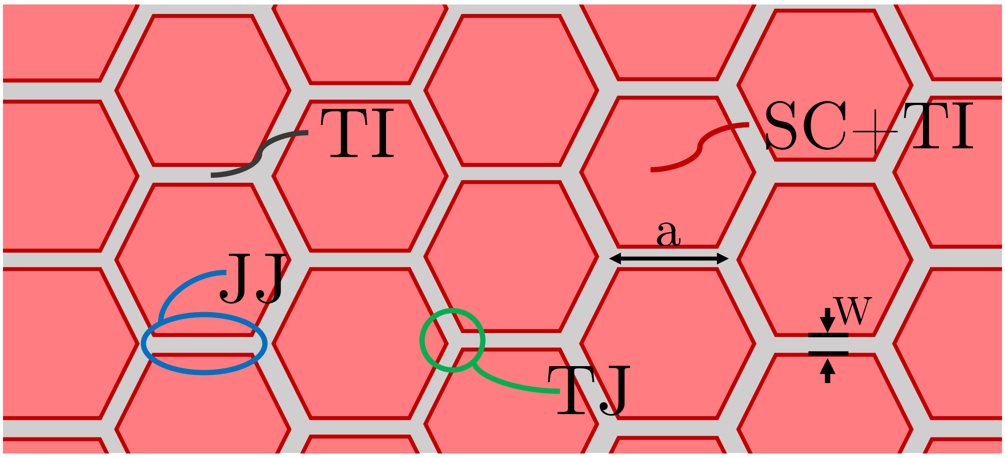

Figure 5.1: Setup of superconducting hexagons on the topological insulator surface and the resulting Majorana wire network. The topological insulator surface (TI, gray background) is proximitized by hexagonal superconducting islands (SC-TI, red). Between the parallel edges topological insulator Josephson junctions (JJ, blue) are obtained, which meet in trijunctions (TJ,green). The length of each Josephson junction is a and the width is W. In the low energy description this setup leads to a network of Majorana wires.

ously [34]. With the phase tiling shown in Fig. 5.2 we will obtain a Majorana bound state at each trijunction. Now we obtained a hexagonal lattice of Majorana bound states. From Fig. 5.2 it is also clear, that neighboring trijunctions never have the same vorticity. The vorticity is equal for all trijunctions of the same sublattice, and the two different sublattices of the hexagonal lattice have opposite vorticity.

Now, we consider a special phase tuning of the superconducting tiles, that leads to a hexagonal lattice with equal interaction between all Majorana fermions.

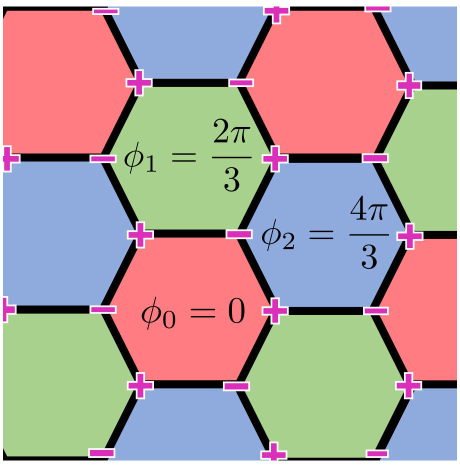

Figure 5.2: Tiling of the pairing gap phases to obtain a Majorana bound state at each trijunction. Each superconducting region is tuned such that every trijunction hosts a Majorana bound state and all conneting Majorana wires have the same gap δ. Each color corresponds to one phase, and this tiling colors the whole plane. The discrete vorticity at each trijunction is indicated by the pink sign and is either $+1$ or -1. The vorticity of neighboring trijunctions is always opposite.

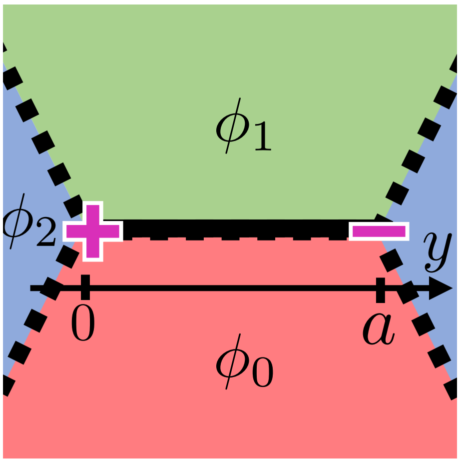

Figure 5.3: Setup of two trijunctions for the calculation of the hopping in the lattice. The vorticity of both trijunctions is non-zero and has opposite sign, therefore the two trijunctions host zero-energy Majorana bound states. The vorticity is indicated by the pink sign. They are coupled by a topological insulator Josephson junction (solid black line), which can be described as a Majorana wire with finite gap. Both Majorana bound states decay exponentially into the wire. They interact through the Majorana wire, and the interaction strength can be calculated by degenerate perturbation theory. The wire coordinate y is indicated. All other Majorana wires at the trijunctions (dashed black lines) are neglected in the calculation of the interaction strength.

We choose the superconducting phases as

$$\phi_j = \frac{2\pi}{3}\, j \quad \text{with} \quad j = 0, 1, 2\,. \tag{5.1}$$

Here the phase differences across each Josephson junction have the same magnitude $|\Delta\phi| = 2\pi/3$, and therefore the gap in each Majorana wire is also of the same magnitude $|\delta_{\text{lattice}}|$.[1] Now the wave function of the localized Majorana mode decays with the same decay length $1/|\delta_{\text{lattice}}|$ into each of the Majorana wires. Since the distance between neighboring trijunctions a is finite, there will be an overlap of the wave functions of different Majorana bound states. This overlap will lead to a small interaction between neighboring Majorana fermions.

To calculate the interaction between neighboring Majorana modes, we consider a setup with two trijunctions and a Majorana wire of length a in between. We tune the superconducting phases according to Eq. (5.1), such that both trijunctions have non-zero discrete vorticity. The setup is shown in Fig. 5.3. Therefore, both trijunctions host a Majorana fermion, but since the vorticity of the two junctions is opposite, the spinor structure has to be different. We choose the coordinate y describing the position in the Majorana wire, such that

[1] For the Majorana wire network it is difficult to define the sign of the phase difference $\Delta\phi$, since it is not clear in which direction we have to measure this difference. If we focus on one individual trijunction of the lattice, we can again define the counter-clockwise direction of phase measurement, but this is not possible for the lattice.

one trijunction is located at $y = 0$ and the other is located at $y = a$ and that the trijunction at $y = 0$ has positive discrete vorticity. The wave functions of the localized Majorana modes are given by

$$\boldsymbol{\xi}^{+} = \frac{1}{\sqrt{N}} \begin{pmatrix} 1 \\ 0 \end{pmatrix} e^{-\hat{\delta} y} \quad \text{and} \quad \boldsymbol{\xi}^{-} = \frac{1}{\sqrt{N}} \begin{pmatrix} 0 \\ 1 \end{pmatrix} e^{-\hat{\delta}(a-y)}\,, \tag{5.2}$$

where the $\pm$ denotes the vorticity of the respective junction, $\hat{\delta}$ is the gap of the Majorana wire, and $N = 3(1 - e^{-a\hat{\delta}})/\hat{\delta}$ a normalization constant of the Majorana modes. The extension of the Majorana bound states into the other Josephson junction at each trijunction can be neglected here. The normalization constant of both modes is identical, since the vorticity of the trijunction only affects the spinor structure and otherwise the bound states at each trijunction are identical. The Hamiltonian describing the Majorana wire is given by

$$H_{\text{wire}} = -iv\,\sigma_x\,\partial_y + \hat{\delta}\,\sigma_y\,. \tag{5.3}$$

For the wire we know that $\hat{\delta} > 0$, since this phase tuning is topologically equivalent to $\Phi_0 = 0$ and $\Phi_1 = \pi - \delta\phi$, where we know the gap perturbatively. With this Hamiltonian as perturbation to the two degenerate Majorana bound states, we can calculate the interaction. The expectation values needed for degenerate perturbation theory are given by

$$\left\langle \boldsymbol{\xi}^{+} \middle| H_{\text{wire}} \middle| \boldsymbol{\xi}^{+} \right\rangle = 0 = \left\langle \boldsymbol{\xi}^{-} \middle| H_{\text{wire}} \middle| \boldsymbol{\xi}^{-} \right\rangle \quad \text{and} \tag{5.4}$$

$$\left\langle \boldsymbol{\xi}^{+} \middle| H_{\text{wire}} \middle| \boldsymbol{\xi}^{-} \right\rangle = -i\,\underbrace{\frac{\hat{\delta}}{3(1 - e^{-\hat{\delta}a})}(v+1)a\hat{\delta}e^{-\hat{\delta}a}}_{=t>0}\,. \tag{5.5}$$

The interaction strength t is always positive, if there is not a topological phase transition in the Majorana wire. It depends on the length a and the gap of the wire $\hat{\delta}$. If the phase fluctuates or the length varies, the interaction strength will vary, but never change sign. However, if there are phase fluctuations present, which induce topological phase transitions in the Majorana wire connecting the two trijunctions, both Majorana modes would vanish. The interaction between the Majorana modes leads to an effective Hamiltonian. With the Majorana creation and annihilation operator $\gamma^{\pm}$ for the two trijunctions it can be written as

$$H_{\text{interaction}} = -2it\,\gamma^{+}\gamma^{-}\,. \tag{5.6}$$

From this elementary interaction, the whole Majorana lattice can be described.

If we consider the total lattice, we get interactions between all Majorana bound states connected by a single Majorana wire. Each interaction takes exactly the form of the two-Majorana interaction. The weak interaction of neighboring Majorana modes is the only possible interaction in the low-energy description of the lattice. Since the interaction is weak, a tight-binding description of the Majorana lattice is valid, where we only have to consider nearest neighbor interactions. If we neglect phase fluctuations of the superconducting phases and assume all Majorana wires to have the same length, the Majorana lattice can be described by

$$H_{\text{lattice}} = -2it \sum_{<n,m>} \gamma_n \gamma_m \,. \tag{5.7}$$

The sum in Eq. 5.7 runs over nearest neighbors, where the Majorana bounds states that interact always are part of different sublattices.[2] We introduce a different notation γ_i^α, where i is a unit cell index and α denotes the sublattice. The Majorana creation operators fulfill the relations given by

$$\gamma_i^\alpha = \gamma_i^{\alpha\dagger} \quad \text{and} \quad \{\gamma_i^\alpha, \gamma_j^\beta\} = 2\delta_{ij}\delta_{\alpha\beta} \,. \tag{5.8}$$

To calculate the spectrum of the Majorana lattice, we introduce Fourier-transformed operators $\tilde{\gamma}_{\boldsymbol{k}}^\alpha$ for both sublattices $\alpha = \pm$ and $\boldsymbol{k}$ in the first Brillouin zone. If r_i^α denote the positions of the lattice sites in sublattice α, the operators $\tilde{\gamma}_{\boldsymbol{k}}^\alpha$ are defined by

$$\tilde{\gamma}_{\boldsymbol{k}}^\alpha = \frac{1}{\sqrt{N}} \sum_{\boldsymbol{r}_i^\alpha} e^{i\boldsymbol{k}\cdot\boldsymbol{r}_i^\alpha}\, \gamma_i^\alpha \,. \tag{5.9}$$

From this definition and the Majorana relations in Eq. (5.8), we obtain

$$\tilde{\gamma}_{\boldsymbol{k}}^\alpha = \left(\tilde{\gamma}_{-\boldsymbol{k}}^\alpha\right)^\dagger \quad \text{and} \quad \left\{\tilde{\gamma}_{\boldsymbol{k}}^\alpha, \tilde{\gamma}_{\boldsymbol{q}}^\beta\right\} = 2\delta_{\alpha,\beta}\, \delta_{\boldsymbol{k},-\boldsymbol{q}} \,. \tag{5.10}$$

With these Majorana annihilation operators in momentum space we can write H_{lattice} as

$$H_{\text{lattice}} = \sum_{\boldsymbol{k}\in 1.\text{ BZ}} -2f(\boldsymbol{k})\tilde{\gamma}_{\boldsymbol{k}}^+ \tilde{\gamma}_{-\boldsymbol{k}}^- \tag{5.11}$$

with

$$f(\boldsymbol{k}) = it \sum_{\boldsymbol{a}_n} e^{i\boldsymbol{a}_n \boldsymbol{k}} \,. \tag{5.12}$$

[2]Here n and m are not the unit cell indices, but they are just two indices, which run over all sites of the different sublattices.

The vectors $\boldsymbol{a}_n$ for $n = 1, 2, 3$ point from a lattice site in sublattice $+$ to the three neighboring lattice sites in sublattice $-$. In momentum space we diagonalize the Hamiltonian by introducing the excitations

$$\tilde{\xi}^{\pm}_{\boldsymbol{k}} = \tilde{\gamma}_{\boldsymbol{k}} \mp \frac{f^*(\boldsymbol{k})}{|f(\boldsymbol{k})|} \tilde{\gamma}^{-}_{\boldsymbol{k}} \, , \tag{5.13}$$

and calculating the commutator $\left[H_{\text{lattice}}, \tilde{\xi}^{\pm}_{\boldsymbol{k}}\right]$. The spectrum is given by $E_{\pm}(\boldsymbol{k}) = \pm 4 \, |f(\boldsymbol{k})|$, which can be expressed in terms of the Cartesian momenta as

$$E_{\pm}(\boldsymbol{k}) = \pm 4t \sqrt{1 + 4\cos\left(\frac{3}{2}ak_y\right)\cos\left(\frac{\sqrt{3}}{2}ak_x\right) + 4\cos^2\left(\frac{\sqrt{3}}{2}ak_x\right)} \, . \tag{5.14}$$

This is exactly the spectrum of graphene in tight-binding approximation with only nearest-neighbor hopping, which is the fermionic version of the hexagonal lattice presented here [35]. We now want to analyze the hexagonal Majorana lattice further and derive transport properties of the lattice. There, we also expect similarities to the graphene lattice. The main difference is, that we do not have electric charge in the Majorana lattice, and therefore we only can measure thermal transport through the Majorana lattice. We have to transform the Majorana lattice, since we will use numerical methods to calculate the thermal conductance of the Majorana lattice and use the Kwant [33] library, which was written for electronic quantum transport problems. In the next section, we will show a mapping between the hexagonal Majorana lattice and a diamond-shaped fermionic lattice. This new lattice can be simulated using Kwant, and the results will be discussed in the last sections of this chapter.

5.2 Transformation into fermionic lattice

In this section we will show how a fermionic lattice can be derived from the hexagonal Majorana lattice. In general we can obtain a fermionic annihilation and the adjoint creation operator from linear combinations of two independent Majorana modes given by

$$c = \frac{1}{2}\left(\gamma_1 + i\gamma_2\right) \quad \text{and} \quad c^\dagger = \frac{1}{2}\left(\gamma_1 - i\gamma_2\right) \, . \tag{5.15}$$

We use this for the transformation of the Majorana lattice by taking the two Majorana fermions of one unit cell of the lattice and constructing a fermionic creation and annihilation operator for each cell out of them. The two Majorana bound states belong to the two different sublattices. If we denote the Majorana

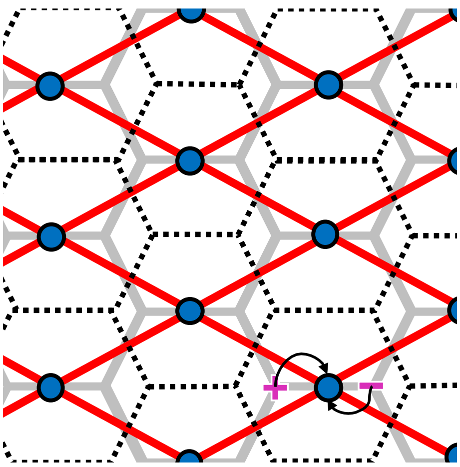

Figure 5.4: Sketch of the transformation to a fermionic lattice structure. The original hexagonal Majorana lattice (gray) is transformed into a fermionic lattice by describing the two Majorana bound states (pink $\pm$) in each unit cell (black dashed line) as a spinless fermionic particle-hole pair. Each pair is located at a lattice site indicated by the blue dots. The unit cells of the lattice are not affected by the transformation. From the transformation to the fermionic description we obtain interaction between cells, which were connected by single Majorana wires in the original hexagonal lattice. The interaction results in hopping in the fermionic lattice and it is coupling particles and holes. The red lines indicate the coupling between the fermionic lattice sites.

bound states with γ_j^α, where j is the unit cell index and α denotes the sublattice, the fermionic operators are given by

$$c_j = \frac{1}{2}\left(\gamma_j^+ + i\,\gamma_j^-\right) \quad \text{and} \quad c_j^\dagger = \frac{1}{2}\left(\gamma_j^+ - i\,\gamma_j^-\right) . \tag{5.16}$$

If we write the lattice Hamiltonian in terms of the spinless fermionic operators, we obtain a new description of the lattice given by

$$H_{\text{lattice}} = -4t \sum_j c_j^\dagger c_j + 2t \sum_{j,n=1,2} \left(c_j^\dagger c_{j+b_n}^\dagger - c_j^\dagger c_{j+b_n} + h.c.\right) , \tag{5.17}$$

where b_n are the lattice vectors connecting the cells, where interaction in the fermionic model is present. Interaction is present only between some nearest neighbors in the lattice, but not all of them. Since we combined the two Majorana operators of each unit cell into a fermionic creation and annihilation operator living on the same site, we obtain an onsite term in the Hamiltonian. The remaining hopping terms of the Majorana lattice result in fermionic hopping terms connecting nearest neighbor sites of the fermionic lattice. Due to the fact that not all adjacent unit cells were connected in the Majorana lattice by Majorana wires, not all nearest neighbors in the fermionic lattice interact. The interaction is only present along the lattice vectors, and if the lattice sites and all interactions are sketched, this results in a diamond-shaped lattice, as

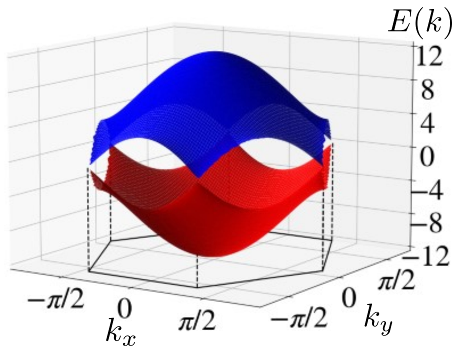

Figure 5.5: The dispersion of the diamond-shaped fermionic lattice is calculated numerically using Kwant. The two energy surfaces (red and blue) are plotted over the first Brillouin zone (black hexagon). The two Dirac cones are located at the corners of the Brillouin zone. The spectrum shown here is identical with the analytical result for the hexagonal Majorana lattice and thus verifies the transformation.

shown in Fig. 5.4.

This lattice can be implemented in Kwant, and we can calculate the spectrum of the diamond-shaped fermionic lattice. If we plot this for the first Brillouin zone, we obtain Fig. 5.5. The spectrum is identical to the analytical result in Eq. (5.14), which verifies the transformation of the lattice.

In later sections, we will consider transport through this fermionic lattice, which we will simulate numerically. We will need periodic and open boundary conditions of the lattice. For the hexagonal Majorana lattice, we consider the so called 'zig-zag' and 'armchair' configurations, which are the two straight regular boundaries. Both are sketched in Fig. 5.6 as well as the orientation and edge shape of the transformed fermionic lattice.[3]

For transport measurements and the scaling of the conductance we will have to consider disorder in the system. As shown in the previous section, disorder can be introduced by considering fluctuations of the phases of the pairing gap or of the length of the Majorana wires. Here, we only consider phase fluctuations, which do not induce a topological phase transition of any of the Majorana wires.[4] In this case the hopping terms in the tight-binding description of the Majorana lattice have to be chosen dependent on the sites. The Majorana

[3]For the fermionic lattice there is a third straight regular edge possible, but this would correspond to dangling bonds in the Majorana lattice, which we do not allow in transport setups.

[4]If we would include such fluctuations, we would have to account for vanishing Majorana modes, since the topological phases of the trijunctions could fluctuate in this case. For this thesis we limit ourselves to the situation where all trijunctions are always in a topological phase.

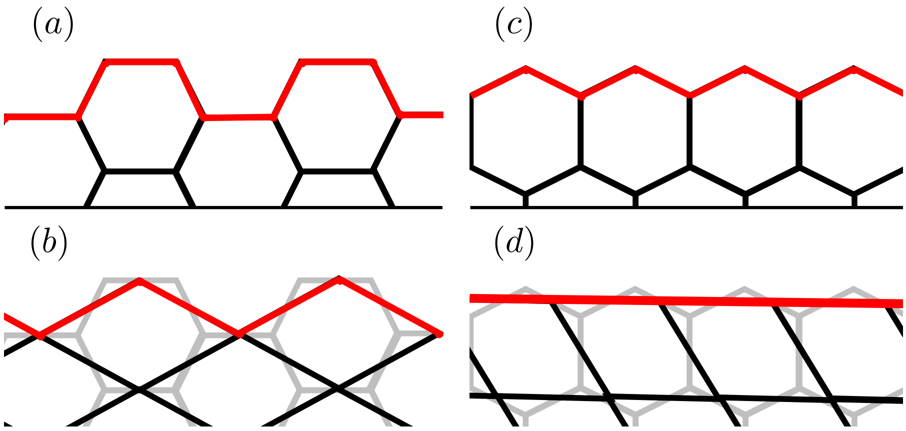

Figure 5.6: Straight regular edges of the Majorana lattice and corresponding fermionic lattice edge. The lattices are always shown in black and the edge in red. For the sketches of the fermionic lattice the original lattice is shown in gray. For the hexagonal lattice there are two straight regular edge configurations. The 'armchair edge' is sketched in (a), and the corresponding edge in the fermionic lattice is shown in (b). The 'zig-zag' edge is sketched in (c), and the corresponding edge in the diamond lattice is shown in (d).

Hamiltonian can be written as

$$H_{\text{disorder}} = -2i \sum_{<i,j>} t_{ij} \gamma_i \gamma_j \,. \tag{5.18}$$

If we transform this Hamiltonian into the fermionic description we obtain

$$H_{\text{disorder}} = -4 \sum_{j} t_j^{\text{onsite}} c_j^\dagger c_j + 2 \sum_{j,n=1,2} t_{j,n}^{\text{hop}} \left(c_j^\dagger c_{j+b_n}^\dagger - c_j^\dagger c_{j+b_n} + h.c. \right) \,, \tag{5.19}$$

where the disorder affects the hopping terms in the Hamiltonian as well as the onsite term. We can simulate this disordered fermionic Hamiltonian to obtain the scaling behavior of the Majorana lattice.

In the next sections we will show the scaling behavior of one-dimensional transport through the Majorana lattice. We will explain the spectra of a Majorana lattice in a ribbon geometry with open and periodic boundary conditions. Additionally, we will analyze the scaling of the conductance for a Majorana lattice junction between two leads. In the final section, we will investigate the scaling behavior of the Majorana lattice in the presence of disorder. All numerical calculations are done using the Python library Kwant, where we always implement the fermionic diamond-shaped lattice derived here.[5]

5.3 One-dimensional transport and edge states

Here we show the one-dimensional transport properties of the hexagonal Majorana wire. We use a ribbon of the lattice with straight regular boundary conditions to calculate the spectrum and show the appearance of edge states for open boundary conditions. Furthermore, we simulate the conductance through a Majorana lattice junction. We connect the Majorana lattice to two normal conducting leads and probe the thermal transport through evanescent modes. We analyze the conductance in the short-wide junction limit and compare our measurements to results for graphene.

If we take a strip of the hexagonal Majorana lattice of length W and expand it periodically into the direction orthogonal to the strip, we construct with an infinite ribbon of width W. In principle, any orientation of the lattice in this ribbon is possible, but we choose it, such that the edges of the Majorana lattice at the ribbon boundary are straight regular. Since the ribbon is periodic in one direction, we obtain a one-dimensional spectrum for the ribbon. The number of modes depends thereby on the width W and on the type of boundary conditions. If we assume first periodic boundary conditions and couple the upper and lower boundary of the ribbon, we obtain the transport spectra shown in Fig. 5.7. Both spectra can be explained as a set of parallel cross sections of the Brillouin zone in Fig. 5.5. The position of the individual cross sections is determined by the different quantized momenta in the direction orthogonal to the ribbon, where the quantization condition is given by the periodic boundary condition. Note that for the zig-zag boundary, we always cut through both Dirac points independent of the width W. The spectrum of the ribbon with the armchair boundary is gapped, and the gap is proportional to $1/W$.

Further we consider a similar situation only with open boundaries. The spectra for this situation are shown in Fig. 5.8. There is no significant change for the armchair boundary, but for the zig-zag boundary an edge state appears. The edge state is not part of the bulk-spectrum and indicates a topological feature of the Majorana lattice. The edge state connects the two Dirac points with a zero-energy mode.

[5] We will not go into any detail concerning the implementation of the lattice or the calculation of spectra and conductance.

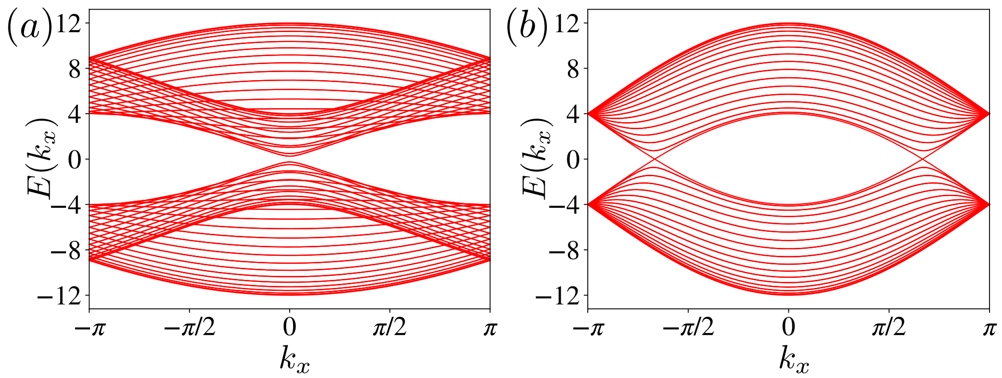

Figure 5.7: One-dimensional transport spectra for Majorana lattice ribbon with periodic boundary conditions. The ribbon has a width of $W = 50a$ with a being the length of the Majorana wires of the hexagonal lattice. The spectra are shown for the two lattice orientations with straight regular edges. Both spectra can be explained as parallel cross sections of the two-dimensional spectrum. In (a), the spectrum for the armchair edge is shown. For this orientation of the lattice the transport spectrum is always gapped. In (b), the spectrum for the zig-zag edge is shown. There, we always cross the Dirac point with one band, and the spectrum is always gapless.

For both types of boundary conditions, the spectra look similar to the ribbon spectra of graphene. Nakada *et al.* [36] showed qualitatively identical spectra for a graphene nanoribbon. This is not surprising, because we already saw, that the bulk-spectrum of the hexagonal Majorana lattice is up to a factor identical to the bulk-spectrum of graphene. Still we have to keep in mind, that the corresponding states and also the edge state are Majorana modes.

We also want to analyze the conductance through a two-dimensional junction built from the hexagonal Majorana lattice. Since the Majorana modes do not carry charge, we cannot probe the charge current, but measure the thermal conductance through the Majorana lattice.[6] Here, we want to measure transport through evanescent modes, meaning the transport through decaying modes inside an energy gap. The gap has to be around zero-energy due to the symmetry of the spectrum. This symmetry is easily shown for the transformed fermionic lattice. The fermionic lattice is superconducting and can be described by a Bogoliubov-de Gennes Hamiltonian, where we again obtain the artificial particle-hole symmetry. Since for the zig-zag boundary we always have modes at the Dirac point, we never have a gapped spectrum and cannot measure transport through evanescent modes. Therefore, we only use the armchair boundary

[6] From now onwards, transport and conductance always denote thermal transport and thermal conductance.

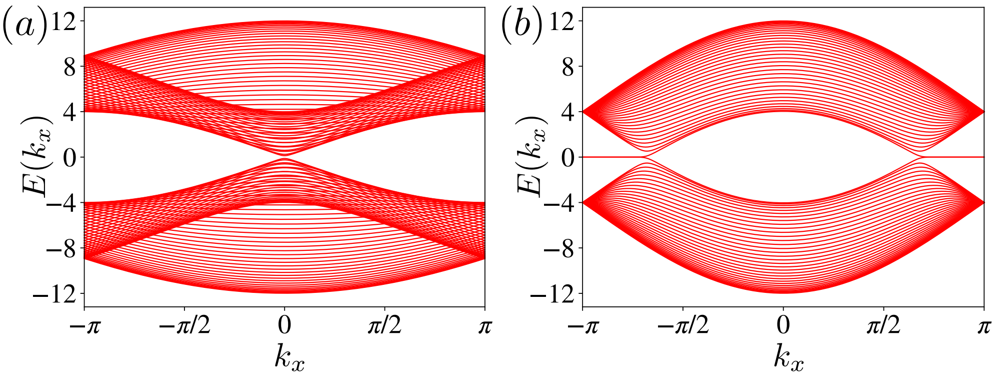

Figure 5.8: One-dimensional transport spectra for Majorana lattice ribbon with open boundary conditions. The ribbon has a width of $W = 50a$ with a being the length of the Majorana wires of the hexagonal lattice. The spectra are shown for the two lattice orientations with straight regular edges. In (a), the spectrum for the armchair edge is shown. For this orientation of the lattice the energy bands shift compared to the periodic boundary condition, but the shape remains similar, and the transport spectrum is always gapped. In (b), the spectrum for the zig-zag edge is shown. Here we do not see the crossings of the Dirac points anymore, which were present for periodic boundary conditions. Instead, an edge state appears, which connects the two Dirac points with a zero energy channel.

for conductance measurements.

We consider a rectangular piece of the Majorana lattice with width W and length L, where we attach normal conducting fermionic leads of width Won both sides. The geometry of the transport experiment is sketched in Fig. 5.9. The leads are tuned, such that we obtain a high density of states at zero-energy, to achieve, that the lead spectrum does not have any influence on the measured conductance. We want to analyze, how the conductance behaves depending on the ratio $R = W/L$. For a fixed width W, we vary L and obtain the results shown in Fig. 5.10. We do not plot the conductance G itself but G/R, which is

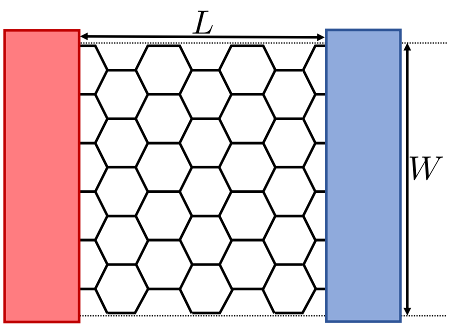

Figure 5.9: Sketch of the setup for the conductance measurement. The hexagonal Majorana ribbon of length L and width W is placed between two normal conducting leads (red and blue). The thermal conductance through the Majorana lattice is measured.

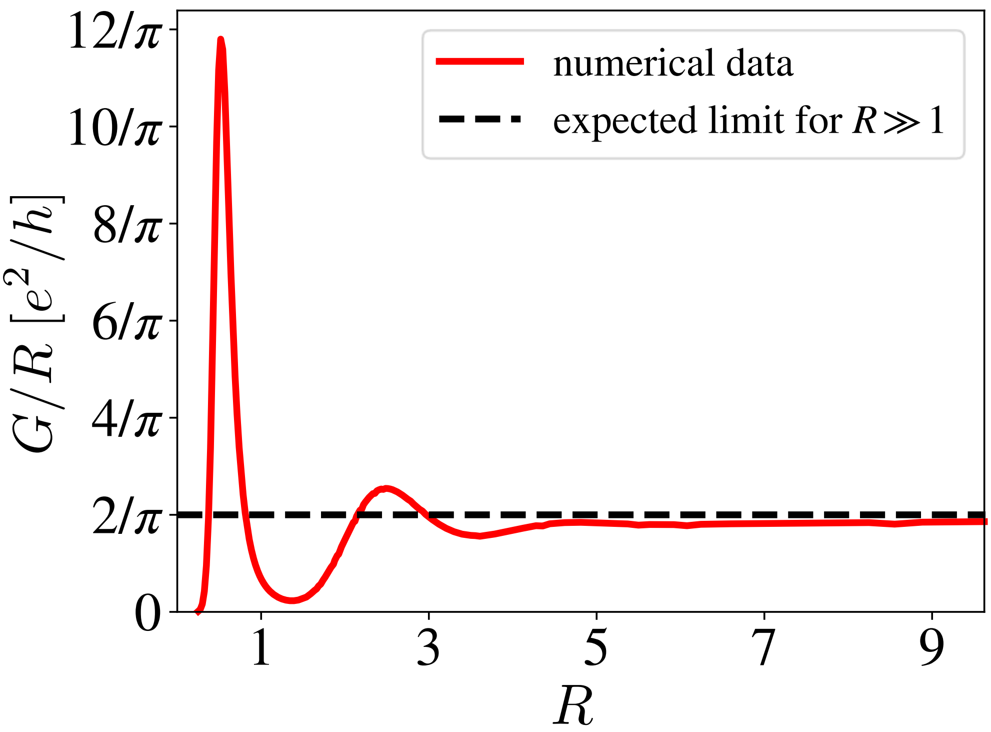

Figure 5.10: Conductance through evanescent modes of the Majorana lattice depending on the ratio of the dimension of the junction. The conductance is plotted over the ratio G/R in units of the conductance quantum against the ratio $R = W/L$ for a Majorana lattice ribbon of width $W = 693a$ with a being the distance between trijunctions in the Majorana lattice. The length L is varied to analyze the scaling of the conductance with R. The limit for $R \gg 1$ is expected due to the similarities between the hexagonal Majorana lattice and graphene, and the value is taken from [37].

the conductivity if Ohm's law holds here. For $R \approx 1$ we obtain large oscillations of G/R, which decay for larger R, until G/R stays constant.

We are mostly interested in the short-wide junction limit $R \gg 1$, where G/R is constant and the conductance increases linearly with R. We want to compare the constant limit of G/R for the Majorana lattice with results obtained for the conductivity of graphene by Tworzydło *et al.* [37]. For $R \gg 1$ they obtained a constant value of $G/R = 2G_0/\pi$ with the conductance quantum $G_0 = 2e^2/h$. In our results, we see a thermal conductivity of the hexagonal Majorana lattice, which is close to $G/R = G_0/\pi$. This value is indicated by the dashed line in Fig. 5.10, and the constant limit of the numerical solution is slightly smaller. It is reasonable, that we only have half of the conductivity in the Majorana lattice, since we only have valley degeneracy for the Majorana lattice and no spin degeneracy, which is present in graphene. Again, the similarities between the hexagonal Majorana lattice and graphene are clear, although we see differences in the behavior of G/R for smaller R and we obtain a small deviation of the expected limit. In [37] the values for G/R do not oscillate around $2G_0/\pi$, but approach this limit from either side depending on the type of boundary condition.

Here we simulated simple transport properties of the hexagonal Majorana lattice and saw edge states appearing in the clean system. Further, we analyzed the thermal conductance through a junction built out of the Majorana lattice and measured a constant conductivity G/R in the short-wide junction limit $R \gg 1$. In the next section, we will analyze the scaling of the conductance in the presence of disorder and obtain contradictions to two-dimensional scaling theory.

5.4 Anomalous scaling of conductance

In this section, we analyze the scaling behavior of the conductance of the hexagonal Majorana lattice in the presence of disorder. Here we calculate the conductance for various systems with increasing system size and investigate, if the the Anderson one-parameter scaling hypothesis holds. The main idea of Anderson scaling was introduced by Abrahams *et al.* in [38], and their key insight was, that the dimensionless conductance $g = G/G_0$ scales as a function of just one parameter. For any disordered system with conductance $g(L)$, where L describes the system size in one, two or three dimensions,[7] the conductance of the scaled system of size αL is given by

$$g(\alpha L) = f_\alpha[g(L)]\,. \tag{5.20}$$

The function depends only on $g(L)$ and is independent of the actual size L, the ratio of the extension in different dimensions, and the disorder strength. This can be formulated elegantly in terms of the so-called β-function, which is given by

$$\beta(g) = \frac{\mathrm{d}\log(g)}{\mathrm{d}\log(L)}\,. \tag{5.21}$$

We are concerned with two-dimensional scaling, and will present consequences of Anderson scaling for general two dimensional systems.

[7] In one dimension the length of the system can be taken as L, and in more than one dimension the extension of the system in each dimension has to be a fixed ratio of L.

We know that for a conductor with $g \gg 1$ Ohm's law holds, and we can estimate the conductance with the classical Drude formula

$$g \propto L^{(d-2)} \implies \beta(g) = d - 2\,. \tag{5.22}$$

This implies that the large conductance limit of the β-function is $\beta(g \gg 1) = 0$ for two dimensional systems. The scaling disappears for all classical contributions, but the quantum corrections remain. Whether the corrections are positive or negative depends on the symmetry class of the Hamiltonian, but the symmetry classification of two-dimensional systems is beyond the scope of this thesis [39]. In general, there are two distinct situations. If the corrections to the classical scaling are positive, disorder leads to higher conductance. The reason for this is that disorder leads to more extended states, which allow for more transport through the system. This behavior is called weak anti-localization. If the corrections are negative, disorder in the system leads to localization of states, which lowers the conductance. However, the localization length of the system is exponentially large. Therefore, the effects of localization only have a small influence on the scaling behavior, and this is called weak localization. We will analyze the scaling behavior of the hexagonal Majorana lattice in the following section and observe contradictions to the scaling theory of two dimensional systems.

For our analysis we choose a specific type of disorder on the hopping in the Majorana lattice, which can be motivated by the microscopic origin of the interaction between nearest-neighbor Majorana modes. The interaction strength for nearest-neighbor modes was calculated before and is given by

$$t = \frac{\hat{\delta}}{3(1 - e^{-a\hat{\delta}})}(v+1)a\hat{\delta}\, e^{-a\hat{\delta}}\,, \tag{5.23}$$

where $v > 0$ is the surface Dirac velocity of the topological insulator, a is the distance between neighboring trijunctions that host Majorana bound states and $\hat{\delta}$ is the gap of the Majorana wire. Only a and $\hat{\delta}$ can vary and the variation of $\hat{\delta}$ results from phase fluctuations of the superconducting regions on the topological insulator surface. We now assume, that the phase fluctuations are small enough to always have non-zero discrete vorticity at all trijunctions on the lattice.[8] With this condition, every trijunction can host a Majorana bound state,

[8]If such strong fluctuations were present, pairs of trijunctions would obtain non-zero vorticity. The two trijunctions would have to have opposite vorticity before, since the sum over

and we never obtain lattice defects in the hexagonal lattice. Another important result is, that the sign of $\hat{\delta}$ is always positive, and thus the interactions are also positive.

For the numerical simulation, we use an approximation of the interaction strength. We focus just on the exponential suppression of t, since here the fluctuations have the largest influence and obtain

$$t \approx t_0 \, e^{\Delta(a\hat{\delta})} \tag{5.24}$$

with $\Delta(a\hat{\delta}) = \langle a\hat{\delta}\rangle - a\hat{\delta}$. Now we assume $\Delta(a\hat{\delta})$ to be normally distributed, which leads to log-normally distributed hopping. We choose the mean value of the distribution, such that we always ensure

$$\langle t\rangle = t_0 \, . \tag{5.25}$$

The variance σ^2 of the log-normal distribution is the measure for the disorder strength. With this distribution for the hopping parameter in the hexagonal Majorana lattice we are able to probe the scaling of the conductance. We use again the transformation into the diamond-shaped fermionic lattice, and implement it using Kwant to obtain the disorder averaged scaling behavior of the conductance. We calculate the scaling both for fixed system size with increasing disorder and for fixed disorder with scaling of the system size.

To probe the scaling of conductance with increasing disorder strength, we choose a system with length $L = 73a$ and the ratio $R = W/L = 4$. We calculate the average conductance for values of σ^2 between 10^{-1} and 10^2 and take the disorder average over $N = 1980$ samples for each disorder strength. The resulting dependence of conductance on disorder strength is shown in Fig. 5.11. Here we immediately obtain the first contradiction to one-parameter scaling, since the scaling cannot only depend on the value of g between average conductance of 1.3 and 2. In this regime of g, there are two different disorder strengths with the same conductance, and the slope of the plotted curve does not have the same sign for these two points. From this follows, that the system scales differently depending on σ^2 and not only g. For the weaker disorder strength with average conductance g the conductance increases with increasing disorder, and for the stronger disorder strength the conductance decreases, even though g is identical in both cases. Therefore, this contradicts the results of one parameter

the discrete vorticity of all trijunctions has to be always 0.

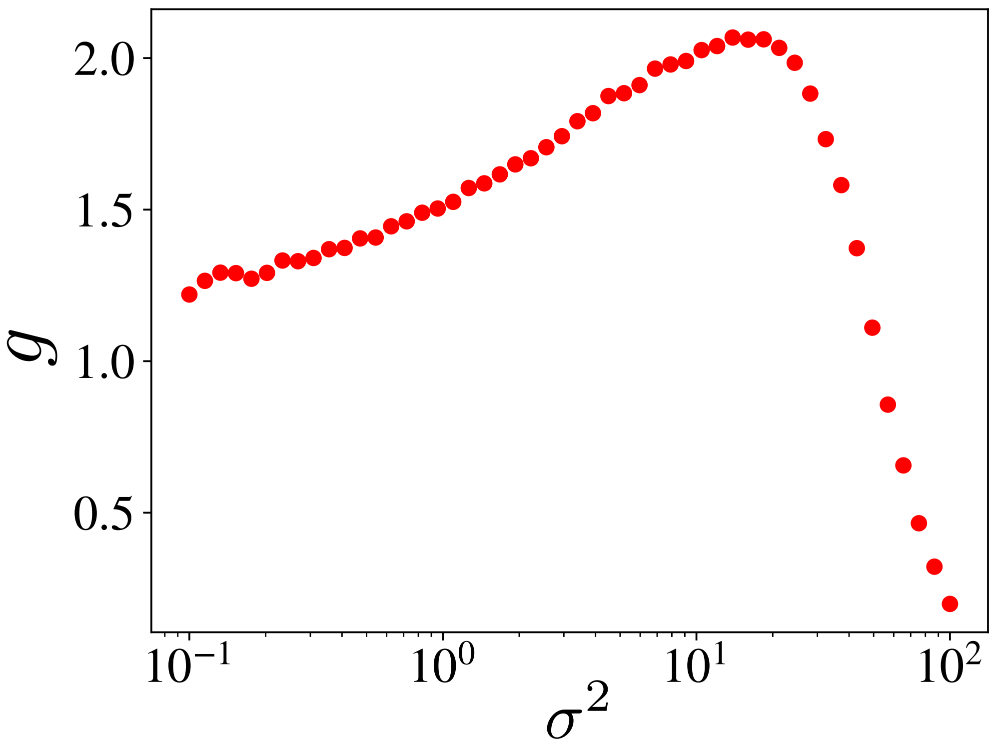

Figure 5.11: Scaling of conductance depending on the disorder strength. The average value of the dimensionless conductance g is plotted against the disorder strength σ^2. The disorder strength is always between 10^{-1} and 10^2. The size of the system is fixed to $L = 73a$ with a being the distance between bound states in the Majorana lattice and $W = RL = 4L$. For each disorder strength the average is taken over $N = 1980$ samples. The uncertainty of the mean value is smaller than the symbol size.

scaling theory and we conclude, that the hexagonal Majorana lattice does not obey Anderson's scaling theory of conductance.

We further want to investigate the behavior for $\sigma^2 < 10^1$, where the conductance scaling could hold, since g is unique for each σ^2. For this regime we see increasing conductance for increasing disorder in Fig. 5.11. If we leave the disorder strength fixed and scale the system $L \to \alpha L$ with $\alpha > 1$, we expect the conductance to increase. The reason for this is, that for one-parameter scaling the conductance should only depend on the ratio of the system size L and the free mean path l^*. The free mean path decreases with increasing disorder strength. Thus, increasing the system size with constant l^* is equivalent to increasing disorder for fixed system size. Therefore we expect the conductance to increase with L for all fixed $\sigma^2 < 10$. If we could define a β-function for this regime alone, the sign should be positive.

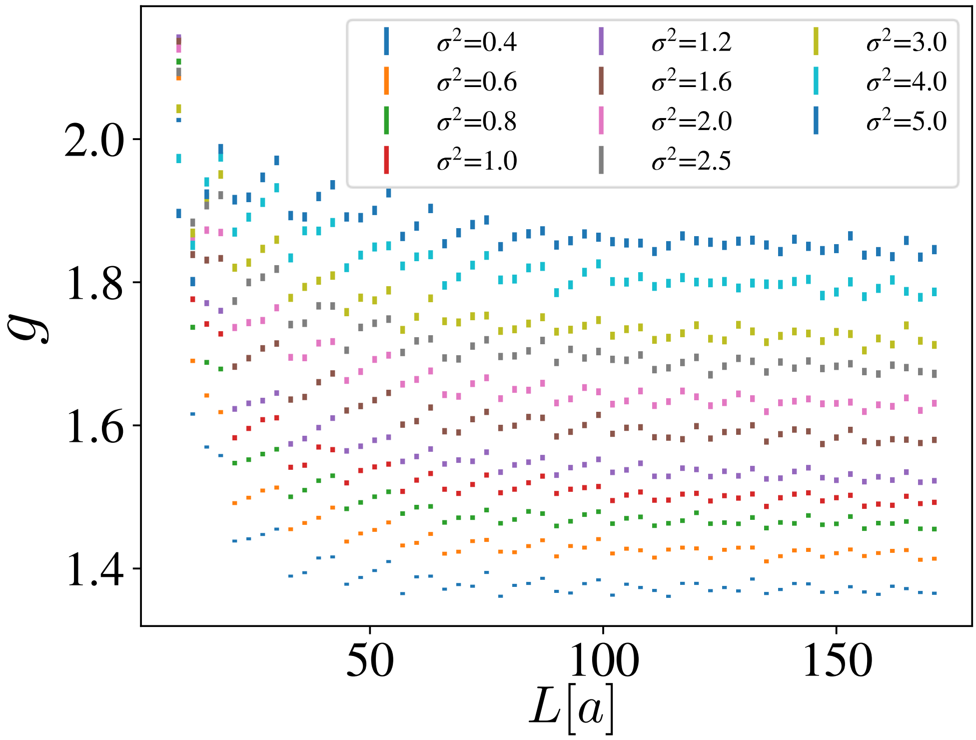

Figure 5.12: Scaling of conductance depending on the system size. The average value of the dimensionless conductance g is plotted against the length L of the system for different fixed values of disorder strength. The ratio $R = W/L$ for the width W of the system is always 4. For each disorder strength and each size the average is taken over $N = 4000$ samples. The uncertainty of the mean value is indicated by the error bar.

To probe the scaling of conductance with increasing system size we vary the length of the system L between $9a$ and $170a$ at a fixed width-to-length ratio of $R = W/L = 4$. The length is increased such that each measured point corresponds to an additional unit cell added in the direction of transport. We calculated the average conductance for values of σ^2 between 0.4 and 5 and took the disorder average over $N = 4000$ samples for each disorder strength at each length. The resulting dependence of conductance on disorder strength is shown in Fig. 5.12.

From the data shown, it is clear, that the conductance decreases with increasing system size, which contradicts the assumption based on our previous results. The scaling behavior for scaling the system size does not match with the scaling behavior for varying the disorder strength for a fixed system size. Further, we see, that the errors on the calculation of the disorder average are so small, that

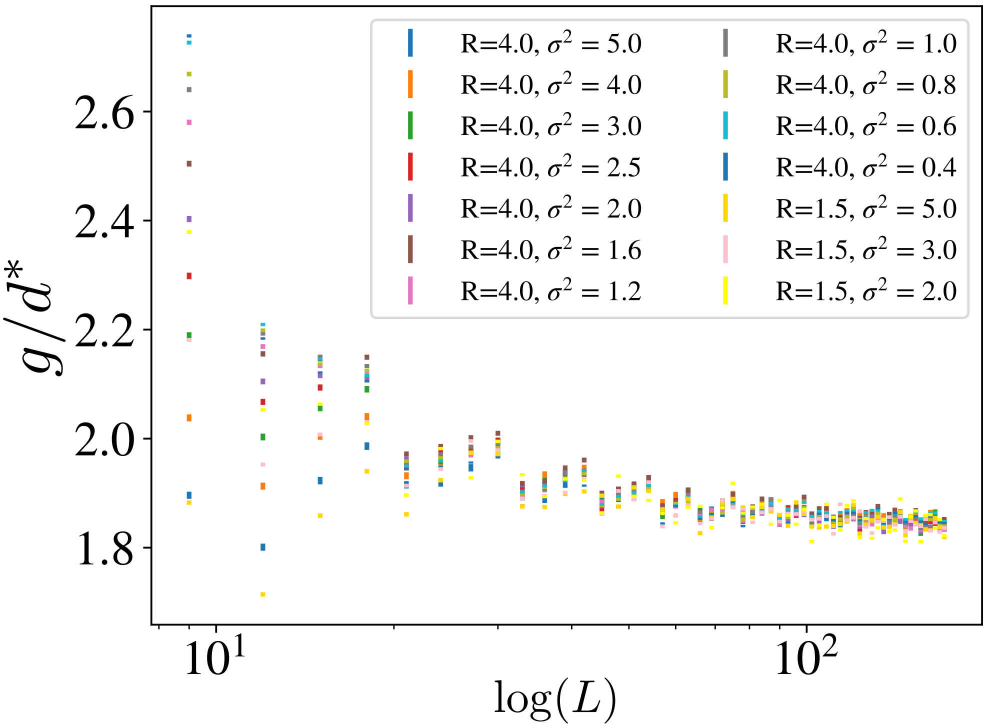

Figure 5.13: Rescaled conductance for different disorder strengths. The average value of the dimensionless conductance g is scaled by a disorder strength dependent factor d^* and plotted against the length L of the system on a logarithmic scale. The ratio $R = W/L$ for the width W varies between measurements. For each disorder strength and each size the average is taken over $N = 4000$ samples. The uncertainty of the mean value is indicated by the error bar. The rescaling is done, such that the points g/d^* fall onto one single curve for larger L. Further the aforementioned four-period rising of the conductance can be seen for all samples for the same lengths.

g does not lay inside the error of values, measured for similar system sizes. This is surprising, because the standard deviation of the individual measurements is large enough to expect reasonable agreement between the average values.

Additionally, we observe some sort of periodic behavior, where the conductance increases over four steps in L and then jumps back down. This trend can be seen for all disorder strengths, even if the free mean path is expected to be far below the system size. It is also notable, that these periods of increasing conductance happen for all disorder strengths for the same values of L. Therefore, we argue, that these rising periods are a lattice effect, and that we should take the average of the four values to analyze the scaling.

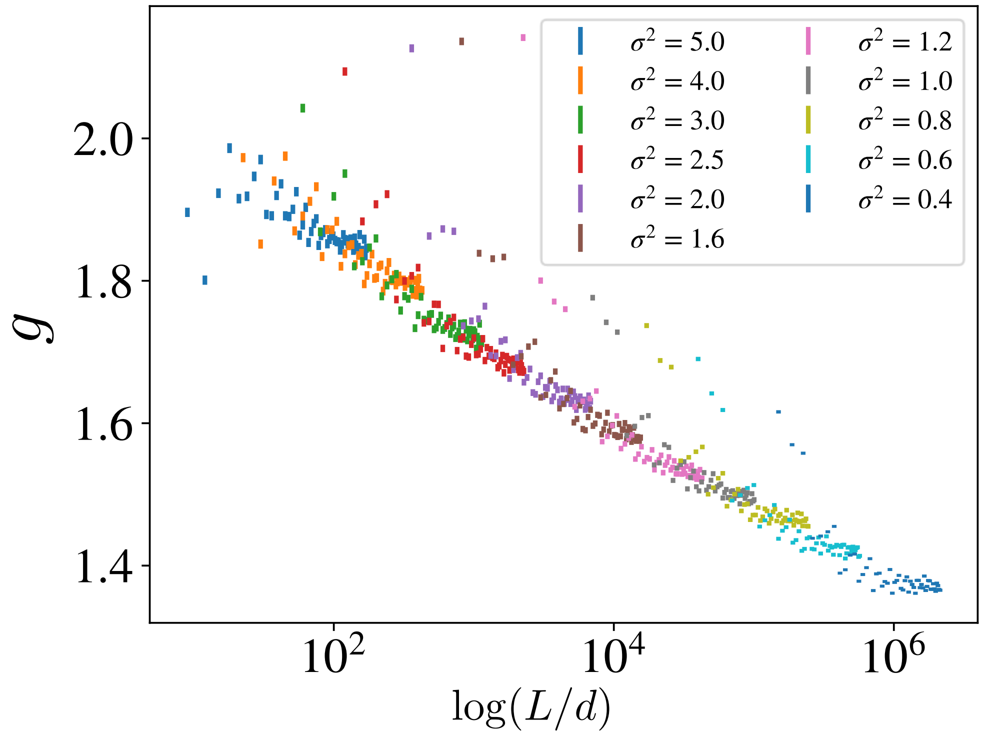

Figure 5.14: Scaling of conductance for limited range of disorder strengths. The average value of the dimensionless conductance g plotted against the length L of the system scaled by a disorder strength dependent factor d. The ratio $R = W/L$ for the width W is always $R = 4.0$. For each disorder strength and each size the average is taken over $N = 4000$ samples. The uncertainty of the mean value is indicated by the error bar. The rescaling is done, such that the points g fall onto one single curve depending on $\log(L/d)$. The points which lie above this curve are the small L measurements for each disorder strength and do not have to lie on the scaling curve.

If we plot the data points on a logarithmic length scale, we notice that the curves can be fitted onto each other by scaling the conductance. We can introduce a disorder strength dependent factor d^* and plot g/d^* against $\log L$, shown in Fig. 5.13. We emphasize, that this is not the usual result for one parameter scaling theory, where we would scale the length and not the conductance. Remarkable is, that we can also scale curves for a different width-to-length ratio $R = 1.5$, and that they fit the data points of the $R = 4$ measurements well. We do not have an explanation for this behavior yet, but are just pointing out the unusual results.

For further analysis of the scaling, we scale the length L with a factor d, while leaving the conductance values unscaled. The scaling factor depends only on

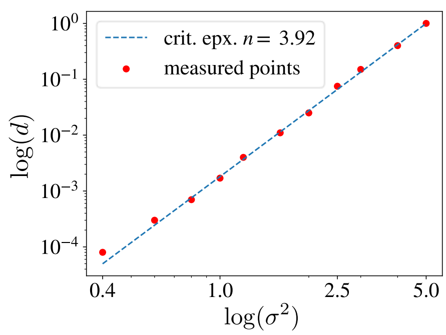

Figure 5.15: Length scaling factor dependent on disorder strength. The scaling factors were determined by scaling length of the system such that the conductance for all disorder strengths falls onto one curve. These scaling factors d are no plotted against the disorder strength σ^2. On the log-log-scale of this plot it is apparent, that the scaling factor depends with a power law on σ^2 and the critical exponent is fitted with $d = c_0\,(\sigma^2)^n$. The fit is shown with the dashed line.

the disorder strength $d(\sigma^2)$, and we obtain a continuous curve for all $R = 4$ measurements. The resulting plot is shown in Fig. 5.14. The thickness of the curve is a result of the aforementioned rising of the conductance over four adjacent data points. For each disorder strength, there are points for small system size, which do not fit the curve, but lie far above. These data points can be explained by the fact, that the scaling theory does not apply for such small system sizes, since the mean free path is much larger than the system size here. Fig. 5.14 confirms, that the β-function over this range of disorder strength is negative, which contradicts the behavior seen for scaling the disorder strength for fixed system size.

To measure how the localization length scales with the disorder strength, we plot the scaling factor d against σ^2 in Fig. 5.15. The scaling factor d grows according to a power law with an exponent of $n \approx 3.92$. We have to point out that this functional behavior $d(\sigma^2)$ only holds for the fixed ratio $R = 4$. For the few measurements done for $R = 1.5$ we would need much smaller values for d to make the conductance g fit the curve in the scaling plot in Fig. 5.14.

Overall the scaling of the conductance yields many results which are not expected from one-parameter scaling theory. There are direct contradictions to scaling theory and it is not possible to define a β-function for the hexagonal Majorana lattice, from the numerical data.

Chapter 6

Conclusion and Outlook

This thesis investigated a hexagonal Majorana fermion lattice created by superconducting islands on a topological insulator surface. After a short introduction into the topic in Ch. 1, we began by introducing Majorana fermions [1, 3] in Ch. 2. There, we showed their rather simple properties and we already demonstrated a decomposition of the Majorana creation operator from 2.1 into fermionic creation and annihilation operators. To explain the emergence of Majorana modes in condensed matter systems, we needed topological concepts, which were also introduced in Ch. 2. After a brief introduction into the field of topology [10], we proved the appearance of a zero-energy mode at a topological domain wall with the Jackiw-Rebbi model [13]. With this model, we were able to calculate the surface Hamiltonian of the three-dimensional Bernevig-Hughes-Zhang model of a topological insulator [8]. Superconductivity also plays an important role in the emergence of Majorana bound states and was introduced here as well. After a short overview of Bardeen-Cooper-Schrieffer theory of superconductivity [20], we explained the proximity effect by Cooper pair tunneling. This led to a finite pairing gap on the topological insulator surface at a insulator-superconductor interface, which can be described by the Bogoliubov-de Gennes formalism [26]. In this formalism holes were introduced to describe the behavior of superconducting systems, and through this we explained Andreev reflection at a superconductor-normal conductor interface. Finally we showed the effect of gauge fields on superconducting systems.

Building on the methods and models introduced before, we constructed a two-dimensional Josephson junction on the surface of a topological insulator in Ch. 3 by proximitizing two regions on the surface with different s-wave superconductors. Similar to results from [7], we were able to show, that for a phase difference of $\Delta\phi = \pi$ across the Josephson junction, there are two zero-energy Majorana modes in the Josephson junction, and we calculated their wave function. The modes decayed exponentially into the superconductors, but could propagate freely along the junction. For a small deviation $\Delta\phi = \pi + \delta\phi$ we calculated the low-energy effective one-dimensional Hamiltonian with degenerate perturbation theory. The resulting Hamiltonian described a topological Majorana fermion wire, where a gap is introduced proportional to $\delta\phi$ and with the sign of the gap as topological invariant. We further analyzed this low-energy description of the Josephson junction in the presence of disorder, and concluded, that any disorder, which preserves the particle-hole symmetry of the system, does not affect the Majorana wire. We also argued, that in the narrow junction limit the presence of the superconductor enforces the particle-hole symmetry and does not allow for perturbations, which would affect the Majorana wire Hamiltonian.

In Ch. 4, we used the topological Majorana wire derived before, to obtain Majorana bound states at topological domain walls. We showed, that these domain walls can only be realized on the topological insulator surface, if we consider trijunctions, where three Majorana wires meet in one point. For this setup we have three tunable phases of the pairing gaps, and we were able to show three distinct topological phases of the trijunction, out of which two hosted Majorana bound states localized at the trijunction. The spinor structure of the Majorana bound state differed between the two phases. We obtained a complete phase diagram of these topological phases and derived the notion of discrete vorticity as a topological invariant of the trijunction. The discrete vorticity can be calculated from the pairing gap phases alone, and the value not only indicates whether a Majorana bound state is present, but also the spinor structure of the respective wave function.

We started Ch. 5 by showing, how infinitely many trijunctions can be connected as a hexagonal Majorana wire network. We proved that there is a special tiling of the pairing gap phases of the hexagonal superconducting regions, which leads to a Majorana bound state at each trijunction. For neighboring Majorana bound states, we calculated a hopping term, depending on the parameters of the connecting wire. This led us to a tight-binding description of the hexagonal Majorana lattice. We were able to calculate the spectrum of the lattice analytically for a situation, in which the hopping over each wire in the network is identical. For numerical simulations of the lattice, we introduced a transformation of the hexagonal Majorana lattice into a superconducting fermionic diamond-shaped lattice, making use of specialized Python libraries for transport simulations.

With this transformation, we were able to verify the spectrum numerically and calculate one-dimensional transport properties. Further, we analyzed the thermal conductance of the hexagonal Majorana lattice and found a constant limit of the conductivity in the short-wide junction limit, which was in accordance with results for the fermionic hexagonal lattice. Finally, we investigated the scaling behavior of the conductance in the presence of disorder and found surprising contradictions to Anderson scaling theory. While scaling the disorder strength, we observed direct contradictions to scaling theory. For regimes of the disorder strength, where scaling seemed to hold, the results of system size scaling and disorder strength scaling were inconsistent.

Overall, we were able to derive a hexagonal Majorana lattice as the low-energy behavior of a superconducting topological insulator surface with hexagonal superconducting regions. We argued, how the Majorana bound states, which form the lattice, are topologically protected if we assume, that the superconducting phase fluctuations are sufficiently small. Simple properties of this lattice could be calculated, but we saw, that the one-parameter scaling approach for the conductance of the lattice seems to fail here. This would have to be investigated further, but our numerical data for the conductance scaling is a good starting point for future research. Furthermore, one could allow for stronger phase fluctuations of the pairing gaps, which would result in lattice defects. The influence of these on the properties of the hexagonal Majorana lattice could also be analyzed. We leave these investigations to future research.

Acknowledgments

First of all, I would like to thank my supervisor Fabian Hassler. He introduced me to Jakob Schluk and Ella Nikodem from the Ando Lab in Cologne, who just presented their work on topological insulator Josephson junctions. Fabian managed to spark my interest on the topic and this was the starting point of my thesis. Over the last year, I learned much from him in our countless discussions. His interest and enthusiasm concerning my work have been a constant source of motivation.

Second, I want to thank Alexander Ziesen, not only for the many discussions on the physics behind my thesis and the much needed ideas for debugging the Python code, but also our fruitful conversations on opening strategies in chess.

Further, I want to thank all former and present members of IQI for creating this nice environment to work in. I would like to thank David DiVincenzo and Markus Müller for the welcoming and relaxed atmosphere at the institute and Helene Barton who easily managed all the bureaucracy concerning summer schools and conferences. In addition to Alex I also want to thank Evangelos and Steven for the countless hours we spend in the office and Lisa who always had time to chat.

I also have to thank Christian, Christoph, Lea, Leon, Malte, Marike and Tobias for taking the time to proof read this thesis.

Finally, I want to thank my parents, my sister Emma and my partner Lea for their constant support and encouragement during the last year. I could always count on them and they somehow managed to make me smile even in the most stressful times.

Bibliography

[1] Ettore Majorana. "Teoria simmetrica dell'elettrone e del positrone". In: *Il Nuovo Cimento (1924-1942)* 14 (1937), pp. 171–184.

[2] Gregory Moore and Nicholas Read. "Nonabelions in the fractional quantum Hall effect". In: *Nuclear Physics B* 360.2-3 (1991), pp. 362–396.

[3] Steven R. Elliott and Marcel Franz. "Colloquium: Majorana fermions in nuclear, particle, and solid-state physics". In: *Rev. Mod. Phys.* 87 (1 Feb. 2015), pp. 137–163. URL: `https://link.aps.org/doi/10.1103/RevModPhys.87.137`.

[4] CWJ Beenakker. "Search for Majorana fermions in superconductors". In: *Annu. Rev. Condens. Matter Phys.* 4.1 (2013), pp. 113–136.

[5] Jason Alicea. "New directions in the pursuit of Majorana fermions in solid state systems". In: *Reports on progress in physics* 75.7 (2012), p. 076501.

[6] K. v. Klitzing, G. Dorda, and M. Pepper. "New Method for High-Accuracy Determination of the Fine-Structure Constant Based on Quantized Hall Resistance". In: *Phys. Rev. Lett.* 45 (6 Aug. 1980), pp. 494–497. URL: `https://link.aps.org/doi/10.1103/PhysRevLett.45.494`.

[7] Liang Fu and C. L. Kane. "Superconducting Proximity Effect and Majorana Fermions at the Surface of a Topological Insulator". In: *Phys. Rev. Lett.* 100 (9 Mar. 2008), p. 096407. URL: `https://link.aps.org/doi/10.1103/PhysRevLett.100.096407`.

[8] H. Zhang et al. "Topological insulators in Bi2Se3, Bi2Te3 and Sb2Te3 with a single Dirac cone on the surface". In: *Nature Physics* 5 (6 May 2009), pp. 438–442. URL: `https://www.nature.com/articles/nphys1270`.

[9] Alexei Kitaev. "Anyons in an exactly solved model and beyond". In: *Annals of Physics* 321.1 (2006). January Special Issue, pp. 2–111. ISSN: 0003-4916. URL: `https://www.sciencedirect.com/science/article/pii/S0003491605002381`.

[10] Xiao-Liang Qi and Shou-Cheng Zhang. “Topological insulators and superconductors”. In: *Rev. Mod. Phys.* 83 (4 Oct. 2011), pp. 1057–1110. URL: https://link.aps.org/doi/10.1103/RevModPhys.83.1057.

[11] R. B. Laughlin. “Quantized Hall conductivity in two dimensions”. In: *Phys. Rev. B* 23 (10 May 1981), pp. 5632–5633. URL: https://link.aps.org/doi/10.1103/PhysRevB.23.5632.

[12] D. J. Thouless et al. “Quantized Hall Conductance in a Two-Dimensional Periodic Potential”. In: *Phys. Rev. Lett.* 49 (6 Aug. 1982), pp. 405–408. URL: https://link.aps.org/doi/10.1103/PhysRevLett.49.405.

[13] R. Jackiw and C. Rebbi. “Solitons with fermion number $\frac{1}{2}$”. In: *Phys. Rev. D* 13 (12 June 1976), pp. 3398–3409. URL: https://link.aps.org/doi/10.1103/PhysRevD.13.3398.

[14] B. A. Bernevig, T. L. Hughes, and SC. Zhang. “Quantum Spin Hall Effect and Topological Phase Transition in HgTe Quantum Wells”. In: *Science* 314.5806 (2006), pp. 1757–1761. URL: https://www.science.org/doi/abs/10.1126/science.1133734.

[15] Alexander Ziesen, Ion Cosma Fulga, and Fabian Hassler. “Geometry-independent tight-binding method for massless Dirac fermions in two dimensions”. In: *Phys. Rev. B* 107 (19 May 2023), p. 195409. URL: https://link.aps.org/doi/10.1103/PhysRevB.107.195409.

[16] H Kamerlingh Onnes. “Further experiments with liquid helium. C. On the change of electric resistance of pure metals at very low temperatures etc. IV. The resistance of pure mercury at helium temperatures”. In: *Through Measurement to Knowledge: The Selected Papers of Heike Kamerlingh Onnes 1853–1926*. Springer, 1991, pp. 261–263.

[17] Walther Meissner and Robert Ochsenfeld. “Ein neuer Effekt bei Eintritt der Supraleitfähigkeit”. In: *Naturwissenschaften* 21.44 (1933), pp. 787–788.

[18] Fritz London and Heinz London. “The electromagnetic equations of the supraconductor”. In: *Proceedings of the Royal Society of London. Series A-Mathematical and Physical Sciences* 149.866 (1935), pp. 71–88.

[19] Leon N. Cooper. “Bound Electron Pairs in a Degenerate Fermi Gas”. In: *Phys. Rev.* 104 (4 Nov. 1956), pp. 1189–1190. URL: https://link.aps.org/doi/10.1103/PhysRev.104.1189.

[20] J. Bardeen, L. N. Cooper, and J. R. Schrieffer. "Theory of Superconductivity". In: *Phys. Rev.* 108 (5 Dec. 1957), pp. 1175–1204. URL: `https://link.aps.org/doi/10.1103/PhysRev.108.1175`.

[21] John Bardeen and David Pines. "Electron-Phonon Interaction in Metals". In: *Phys. Rev.* 99 (4 Aug. 1955), pp. 1140–1150. URL: `https://link.aps.org/doi/10.1103/PhysRev.99.1140`.

[22] David Pines. "Superconductivity in the Periodic System". In: *Phys. Rev.* 109 (2 Jan. 1958), pp. 280–287. URL: `https://link.aps.org/doi/10.1103/PhysRev.109.280`.

[23] P. G. de Gennes. "Boundary Effects in Superconductors". In: *Rev. Mod. Phys.* 36 (1 Jan. 1964), pp. 225–237. URL: `https://link.aps.org/doi/10.1103/RevModPhys.36.225`.

[24] C. W. J. Beenakker. "Random-matrix theory of quantum transport". In: *Rev. Mod. Phys.* 69 (3 July 1997), pp. 731–808. URL: `https://link.aps.org/doi/10.1103/RevModPhys.69.731`.

[25] Rui-Feng Wang et al. "Anomalous superconducting proximity effect of planar Pb–RhPb2 heterojunctions in the clean limit". In: *npj Quantum Materials* 7.1 (2022), p. 116.

[26] Fabian Hassler. *Quantentheorie der Vielteilchensysteme [Quantum theory of many-body systems].* IQI RWTH Aachen university, 2021.

[27] Pierre-Gilles De Gennes. *Superconductivity of metals and alloys.* CRC press, 2018.

[28] Yoichiro Nambu. "Quasi-Particles and Gauge Invariance in the Theory of Superconductivity". In: *Phys. Rev.* 117 (3 Feb. 1960), pp. 648–663. URL: `https://link.aps.org/doi/10.1103/PhysRev.117.648`.

[29] P. W. Anderson. "Coherent Excited States in the Theory of Superconductivity: Gauge Invariance and the Meissner Effect". In: *Phys. Rev.* 110 (4 May 1958), pp. 827–835. URL: `https://link.aps.org/doi/10.1103/PhysRev.110.827`.

[30] M. Titov, A. Ossipov, and C. W. J. Beenakker. "Excitation gap of a graphene channel with superconducting boundaries". In: *Phys. Rev. B* 75 (4 Jan. 2007), p. 045417. URL: `https://link.aps.org/doi/10.1103/PhysRevB.75.045417`.

[31] B. van Heck, S. Mi, and A. R. Akhmerov. “Single fermion manipulation via superconducting phase differences in multiterminal Josephson junctions”. In: *Phys. Rev. B* 90 (15 Oct. 2014), p. 155450. URL: `https://link.aps.org/doi/10.1103/PhysRevB.90.155450`.

[32] N. Read and Dmitry Green. “Paired states of fermions in two dimensions with breaking of parity and time-reversal symmetries and the fractional quantum Hall effect”. In: *Phys. Rev. B* 61 (15 Apr. 2000), pp. 10267–10297. URL: `https://link.aps.org/doi/10.1103/PhysRevB.61.10267`.

[33] Christoph W Groth et al. “Kwant: a software package for quantum transport”. In: *New Journal of Physics* 16.6 (2014), p. 063065.

[34] John H Conway and Jeffrey C Lagarias. “Tiling with polyominoes and combinatorial group theory”. In: *Journal of combinatorial theory, Series A* 53.2 (1990), pp. 183–208.

[35] Gordon W. Semenoff. “Condensed-Matter Simulation of a Three-Dimensional Anomaly”. In: *Phys. Rev. Lett.* 53 (26 Dec. 1984), pp. 2449–2452. URL: `https://link.aps.org/doi/10.1103/PhysRevLett.53.2449`.

[36] Kyoko Nakada et al. “Edge state in graphene ribbons: Nanometer size effect and edge shape dependence”. In: *Phys. Rev. B* 54 (24 Dec. 1996), pp. 17954–17961. URL: `https://link.aps.org/doi/10.1103/PhysRevB.54.17954`.

[37] J. Tworzydło et al. “Sub-Poissonian Shot Noise in Graphene”. In: *Phys. Rev. Lett.* 96 (24 June 2006), p. 246802. URL: `https://link.aps.org/doi/10.1103/PhysRevLett.96.246802`.

[38] E. Abrahams et al. “Scaling Theory of Localization: Absence of Quantum Diffusion in Two Dimensions”. In: *Phys. Rev. Lett.* 42 (10 Mar. 1979), pp. 673–676. URL: `https://link.aps.org/doi/10.1103/PhysRevLett.42.673`.

[39] Takahiro Morimoto, Akira Furusaki, and Christopher Mudry. “Anderson localization and the topology of classifying spaces”. In: *Phys. Rev. B* 91 (23 June 2015), p. 235111. URL: `https://link.aps.org/doi/10.1103/PhysRevB.91.235111`.